Quantitative evolution of the petrophysical properties of andesites affected by argillic alteration in the hydrothermal system of Petite Anse-Diamant, Martinique

Charli Delayre, Patricia Patrier Mas, Paul Sardini, Philippe Cosenza, Anthony Thomas

Quantitative evolution of the petrophysical properties of andesites affected by argillic alteration in the hydrothermal system of Petite Anse-Diamant, Martinique

Charli DELAYRE[a], Patricia PATRIER MAS[a], Paul SARDINI[a], Philippe COSENZA[a,*], Anthony THOMAS[b]

[a]University of Poitiers, UMR CNRS 7285 IC2MP- HydrASA, ENSI Poitiers, France.

[b]University of Poitiers - ISAE-ENSMA, Institut PPRIME, UPR 3346 CNRS, ENSI Poitiers Chasseneuil, France.

***Corresponding author**

Philippe COSENZA

Ecole Nationale Supérieure d'Ingénieurs de Poitiers
Université de Poitiers-CNRS
1 rue Marcel Doré, Bat B1
TSA 41105
86073 Poitiers cedex 09
France
Email: philippe.cosenza@univ-poitiers.fr

Intended for publication in Journal of Volcanology and Geothermal Research

Abstract

The evolution of the petrophysical properties of rocks induced by hydrothermal alteration is often considered qualitatively by sorting the hydrothermal alterations encountered from low to high intensity, depending on the identified mineral paragenesis. In this paper, we studied the evolution of three different petrophysical properties (connected porosity, permeability and electrical conductivity) as a function of the argillization degree of andesites affected by argillic alteration identified in the caprock formation of the Petite Anse-Diamant hydrothermal system in Martinique. These petrophysical measurements were supplemented by quantitative mineral evaluation via scanning electron microscopy (i.e., the Quantitative Evaluation of Minerals by Scanning electron microscopy or the QEMSCAN® method), connected porosity mapping using ^{14}C-PMMA method and measurements of methylene blue (MB) values and structural water proportions (H_2O^+). In the series of rocks investigated, an increasing trend of clay mineral abundances (montmorillonite and kaolinite) from 5.68 to 37.56 % was revealed by the QEMSCAN® method. Based on the quantitative results, the structural water proportions were used as a proxy of argillic alteration progression. Comparison between the mineral maps provided by the QEMSCAN® system and connected porosity mapping observed in autoradiographs using ^{14}C-PMMA method revealed a good correlation with clay mineral phases, dissolution vugs and fractures. The connected porosities evaluated with the triple weight method range from 3.74 to 35.35 % and show a good correlation ($R^2 = 0.8835$) with the H_2O^+ values, revealing that porosity development is mainly due to the replacement of primary phases by clay minerals. In contrast, the crystallization of silica, carbonates and, to a lesser extent, iron oxides tends to clog connected pores, inducing a local decrease in connected porosity, as revealed in autoradiographs. The Darcian permeability ranges from $7.66 \cdot 10^{-20}$ to $5.36 \cdot 10^{-17}$ m² and shows a moderate correlation with the connected porosity. The bulk electrical conductivity measured as a function of the

54 conductivity of the saturating solution reveals the significant contribution of surface
55 conduction arising from montmorillonite. At a pore fluid salinity of 2 wt % (the salinity of the
56 Eaux Ferrées thermal spring), the bulk electrical conductivity shows a relatively good
57 correlation with the H_2O^+ values (R^2=0.8591) and an even better correlation with the MB
58 values (R^2=0.9579). The contribution of montmorillonite to the bulk electrical conductivity
59 was estimated with the use of the isoconductivity point, showing an increase in the BM values
60 and a strong correlation (R^2= 0.9806).
61 **Keywords:** argillic alteration, petrophysical properties, autoradiography, porosity,
62 permeability, electrical conductivity, Petite Anse-Diamant hydrothermal system, Martinique.
63

1. Introduction

Geothermal energy has been of increasing interest in recent decades, notably due to its environmentally friendly character with regard to the low carbon dioxide emissions per kWh produced by geothermal power plants (Kagel and Gawell 2005). In comparison with other energy sources, geothermal energy provides a base load power that is not subject to environmental variables such as sunshine or wind, as are photovoltaic and wind technologies. On the other hand, the main limitations for the development of geothermal power plants are the availability and the capacity of efficiently targeting geological areas with a sufficient local temperature gradient and fluid circulation. These limiting factors could be overcome with the development of enhanced geothermal systems (EGS), seen as the future of geothermal energy by several authors (Tester et al. 2006; Rybach 2010; Gerber and Maréchal 2012). Until this technology is fully operational, the success of finding new geothermal fields is reliant on exploration work intrinsically based on a cross-disciplinary approach with geological, geochemical and geophysical surveys.

Inherent to geothermal systems, hydrothermal alterations are the result of fluid/rock interactions inducing the dissolution of primary minerals of the host rocks and/or the crystallization of a wide range of minerals depending on several factors such as the fluid/rock ratio, time, temperature, pressure, fluid chemistry and permeability (Browne 1978; Roberson and Lahann 1981; Beaufort et al. 1992; Inoue 1995; Patrier et al. 1996; Meunier et al. 2017). Such dissolution and crystallization processes lead to the modification of petrophysical properties such as porosity and permeability, which are essential for the understanding of the hydrogeological dynamics of hydrothermal systems, and in a more practical way, to predict the geothermal reservoir behaviour during exploitation (Pruess 1990; O'Sullivan et al. 2001). Prospecting tools such as electrical and electromagnetic (EM) methods are commonly used for the characterization of geothermal settings as well as to target high-conductivity anomalies

of the subsurface (Komori et al. 2010; Gonzales et al. 2014; Muñoz 2014; Revil et al., 2018a; 2018b; Ahmed et al. 2018; Lévy et al., 2018; Gailler et al., 2019). These anomalies are generally related to the presence of clay minerals resulting from fluid/rock interactions and constitute the so-called caprock formation of hydrothermal systems. The associated high conductivity results from the high cation exchange capacity (CEC) of these minerals, particularly of smectite minerals exhibiting a large amount of cations adsorbed onto their platelet surfaces (e.g., Lévy et al., 2018). However, as Muñoz (2014) reported, the high-conductivity anomalies observed in the field do not always indicate the presence of a caprock and can lead to the incorrect targeting of geothermal wells. Thus, we understand that upfront costs as well as the risk related to the drilling of unproductive wells have a determinant impact on potential investments. Aimed at reducing the risk of unsuccessful wells, laboratory studies investigating hydrothermal alterations and their effects on petrophysical rock properties are essential to better understand the operation of hydrothermal systems and to interpret the data arising from the exploration phase. In the literature, a significant proportion of available papers focuses entirely or partially on the evolution of petrophysical properties depending on parameters such as temperature, pressure and lithology, without taking into account hydrothermal alterations (Björbsson and Bodvarsson 1990; Boitnott and Boyd 1996; Nielson et al. 1996; Dobson et al. 2003; Stimac et al. 2004). It is only recently that hydrothermal alterations are considered qualitatively in parallel with the above-cited parameters for the study of the petrophysical property evolution of volcanic rocks in hydrothermal contexts. Notably, and through several papers, Frolova et al. (2001, 2006, 2010 and 2015) studied the influence of hydrothermal alterations on the petrophysical properties of rocks from the Kuril-Kamchatka island arc by dividing the hydrothermal alterations encountered into low-temperature alterations and high-temperature alterations. Mordensky et al (2019) on their side focused their study on high temperature hydrothermal alterations

developed in Rotokawa geothermal field. Nevertheless, hydrothermal alterations are sorted from weak to high depending on the mineral paragenesis identified usually through optical microscopy observation (Kristinsdóttir et al. 2010; Wyering et al. 2014; Mielke et al. 2015, Nehler et al. 2016, Pola et al. 2012, 2014, 2016, Navelot et al. 2019, among others). Only a few papers quantified clay phases in low temperature environments that constitute upper parts of geothermal systems (Heap et al., 2017, Heap et al., 2020). To date, only papers addressing the electrical conductivities of rocks in geothermal systems have quantitatively considered the impact of clay minerals through empirical relationships, as reported by Ussher et al. (2000) and Caldwell et al. (1986). This is precisely the aim of this paper, where we investigate the effect of clay mineral abundances on the porosity, permeability and electrical conductivity of a series of andesitic samples collected from the caprock formation of the hydrothermal system of Petite Anse-Diamant (Martinique). Moreover, due to the mutual dependence between the porous network and petrophysical properties, autoradiographs of rock sections obtained from ^{14}C-PMMA method will be analysed in parallel with mineralogical maps obtained using Quantitative Evaluation of Minerals by Scanning electron microscopy (QEMSCAN®) to identify the development of the porous network with regard to the mineral phases.

2. Geological settings

Located in the eastern Caribbean Sea, Martinique Island belongs to the Lesser Antilles Island arc, which has experienced volcanic activity from the late Oligocene to the present, as evidenced by the recent and deadly eruptions of Mount Pelée from 1902-1905 and from 1929-1932. The volcanic activity of the entire island arc results from the subduction of the Atlantic plate under the Caribbean plate at a rate of 2-4 cm y^{-1} (Macdonald 2000). Due to its unique position, Martinique Island has recorded the most complete history of the island arc leading to the formation of the following volcanic units, from east to west: the Basal Complex and the

Sainte Anne series; the Vauclin Pitault Chain and the South Western Volcanism unit; and the Morne Jacob, Trois-Ilets, the Carbet Complex, Mount Conil and Mount Pelée, belonging respectively to the old, intermediate and recent arcs (Figure 1) (Germa 2011). The distribution from east to west of the erupted rocks is thought to be related to the penetration of an aseismic ridge under the Caribbean plateau, which led to the flattening of the subducting slab and therefore shifted the volcanic front towards the west (Bouysse and Westercamp 1990). Thus, the western part of the island should be the most suitable region for geothermal exploration due to the potential remnant heat sources allowing the development of geothermal systems. The first investigations on the geothermal potential of Martinique Island were initiated in the late 1960s in the Lamentin area where thermal sources have been recognized (Cormy et al. 1970). Several areas were investigated afterwards during exploration campaigns in the 1980s and 2000s, where the two regions of Mount Pelée and Trois-Ilets showed a strong geothermal potential, particularly the latter, in the area of Petite Anse located in the southwest of the island (Figure 1) (Gadalia et al, 2014-2015).

In the latter area, geochemical analysis of the local thermal spring Eaux-Ferrée revealed a reservoir temperature of 190-210°C, according to chemical geothermometers: Na-Li, Ca-K, Sr-K, Fe-K, 18O(H2O-SO4)) even if the flow rate was low (0.03 l s^{-1}), presumably due to the clayey caprock preventing substantial recharge of the hydrothermal system (Sanjuan et al. 2005; A Gadalia et al. 2014; Coppo et al. 2014). The measured salinity of the latter thermal spring was 20 g l^{-1} (i.e., 2 wt %). This salinity will be used in this article as a reference during the examination of the electrical conductivities exhibited by the sample series. The dating work performed by Germa et al. (2011) allowed to constrain the timeline of the island's volcanic activity and to estimate that the activity in the area of Trois-Ilets occurred between 2.36 Ma and 346 ka ago. At the foot of Morne Jaqueline, where the thermal source of Eaux-Ferrée is located, evidence of the potential existence of a caprock formation has been revealed

by a flank collapse, outcropping andesitic/dacitic rocks affected by argillic alteration with a montmorillonite-pyrite mineral paragenesis associated with zeolite, sulphate, calcite and iron oxides (Genter and Roig 2003; Traineau et al. 2013). Other types of fossil hydrothermal alteration have been recognized in the vicinity of Morne Jacqueline, with notably, a more acidic alteration represented by kaolinite-alunite mineral associations expressing an advanced argillic alteration, characteristic of fumarolic activity (White and Hedenquist 1990, Gadalia et al. 2015). Silica deposits as well as scarce smectite/illite interstratified species have also been identified that should indicate the circulation of past or present fluid flows originating from higher reservoir temperatures. Materials and methods

3.1 Sampling

On the outcrop located at the foot on the side of Morne Jacqueline, a series of 11 samples with an andesitic lithology were collected (Figure 1). To obtain an increasing clay abundance through the whole sample's series, rock samples were collected depending on their apparent consolidation (poorly consolidated = clay rich) and colour, where a grey facies corresponds to low-alteration andesite and lighter/yellowish facies corresponds to a higher argillic alteration progression (Table 1). The detailed petrographic features of the whole sampling is given below section 4.1.

3.2 Quantitative Evaluation of Minerals by Scanning Electron Microscopy (QEMSCAN® analysis)

QEMSCAN® is an automatic quantitative analysis system that allows spatially resolved mineralogical data to be obtained. The system consists of the sequential acquisition of energy dispersive X-ray (EDX) spectra and back-scattered electron images (BSI) of a polished rock section. The raw chemical data obtained are then interpreted using a mineralogical database to associate each measurement point (or pixel) to a mineral. Spatial reconstruction of the

interpreted data leads to a mineralogical image of the rock section investigated. In this work, the mineralogical images as well as the quantitative results acquired from the QEMSCAN® technique will be used to spatially correlate the mineral phases analysed with the connected porosity observed from ^{14}C-PMMA autoradiographs and to study the evolution of petrophysical properties depending on the mineral phases resulting from hydrothermal alteration.

QEMSCAN® analysis was carried out by the ERAMET Research group on 7 thin sections (from samples PA 3, PA 4, PA 7.2, PA 10.1, PA 11, PA 12 and PA 13). Chemical analysis was performed using an FEI Quanta 650 FEG scanning electron microscope mounted with two energy dispersive spectrometers (EDSs) (Bruker; Synergie 4) and a back-scattered electron detector (BSE), operating at an acceleration voltage and current intensity of 15 kV and 5 nA, respectively. The QEMSCAN® software ensured the automatic displacement of the microscope stage with a step size of 10 µm. The acquisition of the X-ray spectrum for each measurement point was considered complete for a total count of 2000 photons. The acquisition time of each thin section was approximately 10 hours. For each area analysed, the recorded EDS spectrum was attributed to one mineral phase by using the Species Identification Protocol (SIP) database (Pirrie et al. 2004; Ayling et al. 2012). To supplement the SIP database results, complementary chemical analysis of the mineral phases was performed in our laboratory using an SEM JEOL 5600 LV operating with a probe current of 1 nA and an acceleration voltage of 15 kV (detector: SiLi EDS AXS Brucker).

3.3 Crystal lattice water abundance (H_2O^+)

Clay minerals are known to embed a significant amount of water in the form of hydroxyls (OH) in their crystal structure. For this reason, the amount of structural water (H_2O^+), generally obtained from bulk-rock chemical analysis, has been used by several authors as an indicator of the weathering grade of rocks (Jayawardena and Izawa 1994a,

212 1994b; Udagedara et al. 2017). In the present study, bulk measurement of the H_2O^+ content is
213 used to support the clay mineral abundances determined from the mineralogical maps of the
214 QEMSCAN® system, and furthermore, we use the H_2O^+ values as proxies for the clay
215 mineral abundances of the whole sample series. The bulk-rock chemical analysis was
216 conducted at the SARM laboratory of Nancy (CRPG, France) on 1 g of each sample,
217 previously ground to reach an average size between 80 µm and 1 mm. The powder samples
218 were heated at 105°C to remove the free and adsorbed water and then placed in an oven at
219 1000°C under a nitrogen atmosphere for determination of the H_2O^+ abundance, following the
220 Karl Fisher titration protocol.

221 *3.4 Methylene blue*

222 Cost-effective and easy to implement, the methylene blue (MB) method can be used
223 during the exploration step of a geothermal project to rapidly evaluate the abundance of
224 smectite minerals on a semi-quantitative basis. The MB method is commonly applied in civil
225 engineering, to estimate the clay content of soils, or to determine the cation exchange capacity
226 (CEC) of clay minerals (Hang and Brindley 1970; Kahr and Madsen 1995; Lorenz 1999;
227 Yukselen and Kaya 2008). MB is an organic dye with the corresponding chemical formula of
228 $C_{16}H_{18}ClN_3S$, which is positively charged when dissolved in water ($C_{16}H_{18}N_3S^+$). Therefore,
229 when the organic dye is added to a suspension containing clay minerals, the cationic dye can
230 be adsorbed onto the negatively charged surfaces as well as onto the interlayer surfaces of the
231 clay minerals. The MB test was conducted by preparing a suspension of 30 cm^3 using 2 g of
232 powder with a grain size of <50 µm. The suspensions were stirred overnight to ensure
233 disintegration of any remaining aggregates. The spot test was performed following the
234 methodology of Santamarina et al. (2002), which consists of adding a methylene blue solution
235 to the sample suspension in increments of 0.5 mL and waiting for 1 min between each MB
236 addition. After 1 min, a drop of the suspension is placed on paper filter to evaluate if all MB

molecules have been adsorbed. When MB molecules are in excess (i.e., all adsorption sites are occupied), a blue halo is formed around the aggregate. The MB value is then calculated from the volume of the MB solution used, $V_{MB\ sol}$, and the mass of the sample (Equation (1)):

$$MB = \frac{m_{sample}}{V_{MB-sol}} \quad (1)$$

3.5 Bulk Connected Porosity

The bulk connected porosity of the samples was evaluated following the triple weight method (TW) (Franklin et al. 1981). The method consists of the measurement of three different weights, depending on the state of the sample: dry, water-saturated and water-saturated suspended in water. Rock pieces of ~10 cm^3 were partially immersed in purified water under vacuum for imbibition. This volume was considered as sufficient in consideration of the representative elementary volume needed for the grain or mineral size distribution of the samples. Any potential fluid excesses present on the sample's surface were removed using a wet paper before measurement of the sample's weight in the saturated state. The saturated samples were dried for 48 h in an oven at 105°C to determine the dried sample weight. The sample bulk volume V_s is calculated using Archimedes' principle by Equation (2):

$$V_s = \frac{w_w - w_a}{\rho_w} \quad (2)$$

w_w is weight of water-saturated sample measured at ambient air. w_a is weight of water-saturated sample plunged in water. ρ_w *is* the mass unit weight of water.

The pore volume V_p is calculated with Equation (3):

$$V_p = \frac{w_w - w_d}{\rho_w} \quad (3)$$

where w_d is the weight of the dried sample.

Finally, the connected porosity φ_{tw} is calculated from Equations (2) and (3):

$$\varphi_{tw} = \frac{V_p}{V_s} = \frac{w_w - w_d}{w_w - w_a} \quad (4)$$

Here, it was assumed that the swelling of expandable clay minerals resulting from the complete water saturation of samples did not significantly influence porosity measurement.

3.6 Connected porosity from the ^{14}C-PMMA method

Bulk measurements of properties such as the electrical conductivity and permeability are intimately linked to the characteristics exhibited by the porous network of rocks (e.g., connectivity, pore type, pore size distribution, anisotropy and tortuosity) (Avellaneda and Torquato 1991; Milsch et al. 2008; Wright et al. 2009). In this section, connected porosity maps of the samples obtained by the ^{14}C-PMMA technique are analysed: (1) to characterize the type of porosity involved in the samples and (2) to analyse the porosity distribution with regard to the mineral phases identified in the QEMSCAN® analysis.

Quantification and imaging of the connected porosity of the samples were performed using the ^{14}C-PMMA methodology developed in the 1990s (Hellmuth and Siitari-Kauppi 1990; (Hellmuth et al. 1993; Siitari-Kauppi 2002). The method consists of measuring the radiation arising from samples saturated beforehand with a ^{14}C-labelled tracer. Polished rock sections of impregnated samples are put into contact with an autoradiographic film (FA) composed of an emulsion of silver bromide crystals (AgBr) of which the Ag^+ cations can be reduced to metallic silver by absorption of the electrons arising from the ^{14}C-labelled tracer. The latter process results in a blackening of the autoradiographic film corresponding to the distribution of the radionuclide tracer and therefore the connected porosity. After exposure, the autoradiographic film is developed and digitized for image analysis. In this study, core samples with dimensions of 4 cm in diameter and 3 cm in height were dried in an oven at 40°C for one month and placed under vacuum for three hours to remove any residual water. Impregnation of the samples with a ^{14}C-MMA solution of an activity of 178 kBq mL^{-1} was performed under vacuum for one month at the Laboratory of Radiochemistry (Helsinki, Finland). Polymerization of the ^{14}C-MMA solution in the porous network was ensured by

heating the sample in a bath at 55°C for 16 hours. Finally, the impregnated samples were sawed and polished to ensure the optimal contact between the autoradiographic film and the rock sections. The autoradiographic films used in this work were KODAK BioMax MR films (resolution: 20 μm) for a total exposure time of ~4 days. Digitization of the autoradiographic film into grey-level 16-bit depth images was performed using a Microtek Artix Scan F1 scanner with a resolution of 2400 dpi (pixel size: 10.6 μm). Due to the non-linear response of the autoradiographic film to irradiation, 14 standards of pure ^{14}C-PMMA with known activities were exposed at the same time to provide an empirical relationship between the blackening of the film and the connected porosity. However, the maximal range of electrons emitted by the ^{14}C in PMMA has been estimated by Kanaya and Okayama (1972) at ~224 μm, which is significantly higher than the thickness of the thin sections used for the acquisition of the autoradiographs (~30 μm). Following this condition and since the thickness of the ^{14}C-PMMA plugs used as standards for the calibration have a thickness on the order of a few millimetres, the porosities calculated from the calibration process are underestimated. Table 2 provides an overview of comparison of ^{14}C-PMMA porosity method with more popular imaging methods, such as Scanning Electron Microscope (SEM) and X-Ray Computed Microtomography (XRCT). Other class of methods provide pore size distribution (Hg-porosimetry and adsorption methods), or provide merely bulk porosity value (TW method and He-pycnometry). The main advantage of ^{14}C-PMMA method consists on his ability to provide quantitative porosity maps which are easy to analyse, and which account all connected pores of the studied section, regardless of pore size (it is why this method is sometimes called multi-scale). For instance, concerning microcracks, the method is able to map at core scale all cracks, whatever their aperture (Mazurier et al., 2016; Bonnet et al., 2020). This is not the case for XRCT or SEM, which does not provide porosity maps, but where pore can be detected by image segmentation. The smaller pores are not detected using

these methods because their size are smaller than pixel or voxel size. In fact, for these conventional imaging methods, the resolution is a function of the sample size, controlling the pixel or voxel size. ^{14}C-PMMA has his own drawbacks, such as the need to manipulate open radioactive sources, and the fact that it is not 3D (Table 2). However, the cost remains the same than XRCT, and the total analysis time is also quite comparable to other porosimetric methods. As emphasized by Table 2, the bulk methods have not to be ignored, because they provided reference values for porosity calculation.

3.7 Intrinsic Water Permeability

We used here the same device employed by Sardini et al. (1996), except that core samples with a diameter of 35 mm were covered on their side with LOCTITE EA 9483 epoxy resin to avoid any lateral leakage of water during the permeability experiment. The high viscosity of this epoxy resin prevents intrusion in the pore space of the samples. The thicknesses of the core samples range from 10 to 15 mm. The sample thicknesses were large compared to rock grain size in order to have a measurement representative of the whole rock. Large phenocrysts of feldspars or hornblende can be however the same size as the sample thickness used for these measurements. It was not possible to use thicker samples because the maximal thickness acceptable by the used device is 2.5 cm. Figure 2 shows the experimental setup for the permeability measurement.

Permeability experiments were performed in steady state flow conditions, using a pressure gradient (ΔP) kept between 1 and 2 bar across the samples. Two nitrogen reservoirs imposed the up and downstream pressure into the H_2O vessel (Figure 2). These reservoirs were isolated from the water circuit by an impervious membrane; the pressures imposed by the inflation of these N_2 reservoirs provided the pressure gradient necessary to the flow of water through the rock sample. The differential pressure was recorded during the experiment, and the flow rate of water was measured using a capillary (Figure 2). The experimental flow

rate being very low (ranged between 0.7 to 4x10^{-4} mm^3/s), the permeability was calculated assuming a laminar flow regime, using Darcy's law:

$$k = \frac{Q\eta l}{S\,\Delta P} \quad (5)$$

where k is the intrinsic permeability (m²), Q is the measured flow rate (m^3 s^{-1}), η is the dynamic viscosity (Pa.s), S is the surface area of the plug sample corrected from the impregnation resin (surface efficient for the water flux) (7.07 10^{-4} m²) and l is the length of the core sample.

3.8 Electrical conductivity

Electrical measurements were performed with a Solartron Impedance Analyser 1260 using 6 NaCl brines with increasing salinity levels of 0.01; 0.05; 0.1; 0.5; 1 and 2 wt %. Note that the range of salinities used encompasses the range of total salt concentrations commonly found for geothermal fluids (0.1 – 1 wt %) (Henley and Ellis 1983). Sample saturation was performed at 20°C by immersion in NaCl brines for two weeks.

A resistivity cell of Teflon was designed to receive the plug samples used for the permeability measurements (Figure 3). After placing the plug sample in the resistivity cell, NaCl brine was added through the two upper apertures of the cell to ensure electrical conduction between the electrodes and the surface of the plug sample. Acquisition of the impedance spectra was performed with the two-electrode configuration in the 0.1 - 3·10^6 Hz frequency range. The conductivity magnitude $|\sigma|$ was obtained with following Equation (6):

$$|\sigma| = \frac{1}{|Z|}\frac{l}{S} \quad (6)$$

where the impedance amplitude |Z| has been selected at a frequency close to 1 kHz (e.g., Lévy et al., 2018) for which the imaginary part of the complex impedance Z was minimum. For

358 simplicity in writing, the conductivity magnitude, $|\sigma|$, will be simply named the electrical
359 conductivity, σ, hereafter.

360 **4. Results and discussion**

361 *4.1 Progression of hydrothermal alteration*

362 The hydrothermal alteration exhibited by the sample series has already been discussed
363 thoroughly in a previous article (Delayre 2018). In this article, we report the main results and
364 petrographic features of the samples that we believe play a significant role in the evolution of
365 the petrophysical properties investigated.

366 Figure 4 presents selected areas of the mineral maps obtained in the QEMSCAN®
367 analysis of samples PA 13 and PA 4 and PA 7.2, PA 10.1, PA 12 and PA 11. For the whole
368 sample series, the mineral phases identified in the QEMSCAN® analysis consist of feldspar
369 minerals belonging to the plagioclase series (andesine, labradorite, oligoclase and bytownite),
370 hornblende and quartz, corresponding to primary minerals, while alteration paragenesis is
371 represented by clay minerals (montmorillonite and kaolinite), iron oxides, carbonates and
372 sulphide minerals. The matrix of the rock with the above-mentioned primary minerals
373 embedded corresponds to a mesostasis where feldspar microlites and devitrification of glass
374 have been observed using optical microscopy in a previous work (Delayre 2018). The
375 alteration paragenesis exhibited by the samples is very common in hydrothermally altered
376 volcanic rocks and can be identified as argillic alteration (White and Hedenquist 1990;
377 Pirajno 2009). From a more petrographic point of view, the size of the feldspar and
378 hornblende crystals ranges from the sub-millimetre to the millimetre and frequently exhibit
379 rectangular and sub-hexagonal sections, respectively (Figure 4). The lowest alteration
380 intensity is observed in sample PA13, which has been discriminated as two different samples,
381 PA13.1 and PA13.2, where the latter corresponds to the wall-rock area of small fractures

characterized by higher abundances of silica and iron oxides, as observed during field sampling (arrows 1 and 2, respectively, sample PA13.2 in Figure 4). Crystallization of montmorillonite produces a patchy alteration pattern in the mesostase along with a moderate alteration of hornblende crystals, as shown in the PA 13.1 sample (arrow 3, Figure 4). Intragranular alteration of hornblende crystals is clear in the PA 4 sample, where montmorillonite crystallizes in association with the iron oxide phases along hornblende cleavages intersecting at 120° (Figure 4). Among the samples investigated, a particular feature is found for PA7.2, where a vein of predominantly montmorillonite is observed and crosses the entire sample (Annex 1). In Figure 4, the PA10.1 sample exhibits a higher alteration intensity revealed by the stronger pervasiveness of alteration of montmorillonite and silica present throughout the mesostase and hornblende crystals, which, for this sample, are completely replaced by montmorillonite and sulphide minerals (± silica ± iron oxides) (arrows 1 and 2, respectively; Figure 4). The strong association of montmorillonite and sulphide minerals is not systematic throughout the sample series investigated and should reveal either a chemical variation in fluid composition affecting the rocks or local variation in the pre-existing lithology. Such variation in fluid composition is supported by the crystallization of carbonates, with calcite as the major mineral phase, manifested as infilling of fractures and dissolution vugs in sample PA10.1.

Strong pervasive alteration is observed in the PA 12 sample, where at this stage, complete replacement of the hornblende crystals by montmorillonite, strongly associated with iron oxides, is observed (arrow 1, PA 12, Figure 4). Dissolution of the mesostase as well as of feldspar minerals is revealed by the increased number of white pixels corresponding to porosity in the mineral maps obtained in the QEMSCAN® analysis. At this stage, only quartz crystals remain unaffected by hydrothermal alteration.

406 With regard to the alteration intensity, the end member of this sample series is represented by
407 PA 11, where intense pervasive alteration is observed (Figure 4). In addition to the total
408 replacement of the hornblende crystals by montmorillonite and silica (± kaolinite) (arrow 3,
409 PA 11, Figure 4), the PA 11 sample presents frequently open cavities resulting from the
410 quasi-total dissolution of feldspar crystals in which few remnants can still be observed (arrow
411 2, PA 11, Figure 4). This dissolution vugs are often completely or partially filled with
412 kaolinite and silica and to a lesser extent with montmorillonite (arrow 1, PA 11, Figure 4). In
413 this last sample, such a strong occurrence of kaolinite could be attributed to advanced argillic
414 alteration resulting from the circulation of more acidic (low pH) fluids. However, the absence
415 of minerals such as alunite, typical of advanced argillic alteration, and the low crystallinity of
416 kaolinite revealed by X-ray diffraction (XRD) analysis could indicate a weathering origin
417 (Hughes, 1980; White and Hedenquist, 1990; Delayre, 2018).

418 *4.2 Quantitative evaluation of hydrothermal alteration*

419 The quantitative results obtained in the QEMSCAN® analysis are presented in Table 3, in
420 which samples were ranked from left to right with increasing clay mineral abundances.
421 Overall, good agreement is found between the quantitative results and the qualitative
422 characterization performed in the previous section. The abundance of feldspar minerals is
423 relatively stable throughout the sample series, varying between 30 and 40 %, except for the
424 PA12 and PA11 samples, which display abundances of 23.31 and 4.27 %, respectively, due to
425 the partial or total dissolution of feldspar crystals. Feldspars are the main source of alumina
426 for montmorillonite and kaolinite. This explain their decreasing amount as the alteration
427 degree increases. This replacement is confirmed by the shape of montmorillonite aggregates
428 as observed in PA11 (rectangular sections in Figure 4).The raw quantitative results do not
429 seem to reflect the replacement or dissolution of the mesostase. However, a general

decreasing trend is found when abundance recalculation is performed considering the white pixels in the mineral maps.

As observed in the mineral maps, only the PA 13.2 sample, the least argillized of the sample series, shows a high abundance (13.9 %) of hornblende, where due to the higher alteration intensity, this value falls below 1 %. Nevertheless, no significant trend of hornblende abundance can be found with increasing amounts of clay mineral phases, as depicted by the PA10.1 sample exhibiting a hornblende abundance of 0.1 %, considered moderately argillized. The abundances of carbonates and iron oxides are low (i.e., < 3 %) and erratic throughout the sample series even though PA13.2 presents a slightly higher iron oxide abundance. With regard to the major hydrothermal alteration products, both kaolinite and montmorillonite are ubiquitous in all samples, where for the latter, an increasing trend from 4.69 to 22.74 % is observed. For the former, the abundances are systematically below 1 %, with the exception of samples PA 12 and PA 11, which display abundances of 3.92 and 14.82 %, respectively.

As mentioned in the materials and methods section in this study, only certain samples of the whole series were selected for QEMSCAN® analysis. Thus, to include the remaining samples in the petrophysical analysis, the abundance of structural water in each sample was determined in view of using its value as a proxy for the clay mineral abundance. The results are presented in Table 4 and Figure 5, where the total clay mineral abundances are plotted against the H_2O^+ values obtained from the bulk-rock chemical analysis.

A good and linear correlation is found (R^2= 0.9854) between the total clay mineral abundances and crystal lattice water proportions, which therefore confirms the assumption established previously. However, such indicators should be handled carefully when used for the semi-quantitative evaluation of clay minerals. Indeed, several hydrothermal minerals (e.g.,

454 the zeolite group, alunite, epidote, pyrophyllite) can also exhibit embedded water in their
455 crystalline structures and therefore may bias the results if used without caution.

456 *4.3 Comparison of the mineral maps and autoradiographs from the ^{14}C-PMMA method*

457 Figure 6 presents the mineral maps of the PA13, PA4, PA10.1, PA12 and PA11 samples
458 in parallel with autoradiographs of the same areas. Notably, several fractures undetected by
459 microscopy are clearly revealed by the autoradiographs of samples PA13, PA4 and PA10.1.
460 For the first two samples, PA12 and PA14, no significant infilling or evidence of fluid-rock
461 interactions in the vicinity of the microfractures was observed in the mineral maps. This could
462 indicate that the generation of the observed microfractures was posterior to hydrothermal
463 alteration. Conversely, deposition of iron oxides as well as carbonates was observed in the
464 main fracture and in the dissolution vugs. The PA10.1 sample revealed that these structures
465 were used as pathways for hydrothermal fluid circulation. In the autoradiographs, such
466 crystallization of carbonates is associated with low porosity areas, as observed in the PA10.1
467 and PA12 samples (arrow 3 and arrow 2 in Figure 6). Additionally, deposition of silica (and
468 presumably of iron oxides) tends to have a similar impact by clogging the connected pores
469 and therefore reducing the overall average porosity of the rock. This process is particularly
470 notable for the PA13 sample, where, in the autoradiographs, a large porosity contrast is found
471 between PA13.1 and PA13.2, displaying silica abundances of 4.91 and 8.64 %, respectively
472 (Table 3). The sulphide minerals are also congruent with the low porosity areas when infilling
473 dissolution vugs or in pseudomorphosed hornblende crystals (arrow 1, PA10.1, Figure 6).

474 Overall, an increasing trend of the connected porosity is found for the whole sample series
475 when calculated from the autoradiographs (Table 4), although underestimated, as explained in
476 section 3.6. In the autoradiographs presented, the porous areas are associated mainly with the
477 clay mineral phases, dissolution vugs and fractures and are visible as dark areas in the
478 autoradiograph. Notably, montmorillonite crystallizing along hornblende cleavages is

associated with porous areas (darker) as clearly revealed by the autoradiograph of the PA 4 sample (arrow 1, Figure 6). Destabilization of the mesostase through dissolution and replacement by mineral paragenesis leads to a global porosity increase of the rock matrix where even the pseudomorphosed hornblende crystals are difficult to discriminate from the rock matrix (arrows 3 and 1 for PA12 and PA11, respectively, Figure 6). Conversely, the dissolution vugs associated with feldspar crystals in PA11 are clearly distinguished from the rock matrix (arrow 2, PA 11, Figure 6). Infilling of kaolinite, observed in the same feldspar crystal, seems to reduce the porosity. Only quartz crystals remain unaffected by hydrothermal alteration and can be easily observed due to their lower porosity (arrow 3, PA11, Figure 6).

4.4 Evolution of the bulk connected porosity and intrinsic permeability

Figure 7 (A) presents the evolution of the connected porosity estimated from the triple weight method as a function of the structural water proportion (H_2O^+), used in this study as a proxy of the clay mineral abundance. The connected porosities of the samples range from 3.74 to 35.35 % and show strong linear relationships with the H_2O^+ values (R^2= 0.8835), revealing that in the rock series investigated, the dominant process of porosity creation is related to the crystallization of clay minerals (i.e., montmorillonite and kaolinite). Moreover, the silicification and crystallization of iron oxides reported above for sample PA13.2 compared to PA13.1 seems to have a great impact on the connected porosity, inducing a decrease from 10.5 to 4.48 %. The moderate scattering of porosity data at low H_2O^+ values is attributed to the presence of fractures and dissolution vugs causing an increase in connected porosity, as observed for the PA10.1 sample.

The intrinsic permeabilities measured for the sample series, ranging from 7.7 10^{-20} to 5.4 10^{-17} m^2, show an increasing trend with the connected porosities measured by the TW method (Figure 7, B). The highest permeability value is found for the PA11 sample and seems unexpected since this sample is the most argillized among the samples in the present series.

504 This finding should be related to the strong destabilization of the rock matrix as well as to the
505 dissolution vugs developed at the expense of the feldspars, as observed in the mineral maps
506 and autoradiographs. Numerous data of permeability reported in the literature for effusive
507 andesites (Wright et al., 2009, Farquharson et al, 2015, Mielke et al, 2015, Heap and
508 Kennedy, 2016, Heap et al., 2018, Mordensky et al, 2018 among others) exhibit a range of
509 permeability from 10^{-17} to 10^{-11} m². Nevertheless lower values down to 10^{-19}-10^{-20}m^2 are also
510 mentioned (Wollentz and Heiken, 1992; Petrov et al, 2005; Navelot et al, 2018). It should be
511 noted that most of the values reported in the literature are gas permeabilities. Other data can
512 be found in the literature on lavas or lavas block of various compositions (Bernard et al., 2007
513 ; Dobson et al, 2003; De Maisonneuve et al, 2009 ; among others) or on pyroclastic materials
514 (Degruyter et al., 2010 ; Heap et al., 2017 ; Heap et al., 2020). The permeability data reported
515 in the literature are 2 to 4 orders of magnitude higher than the permeabilities measured in this
516 work. Part of this shift could be explained by the fact that permeability values found in the
517 literature are mainly gas permeability while in the present study we determined water
518 permeability. This latter value is probably closer to real permeability in natural systems
519 affected by smectitic alteration. Indeed smectitic material consists in expandable clay phases
520 which can strongly affect the permeability in water saturated conditions. As an illustration in
521 Krafla system, Escobedo (2018) observed 2-3 orders of magnitude between gas and water
522 permeabilities in hyaloclastic formations affected by smectitic alteration. From this
523 observation, we deduce that hydrothermal alteration induces a consequent decrease in the
524 permeability (at least one order of magnitude) due to the formation of expandable clay
525 minerals. The subsequent dissolution of the rock matrix and pre-existing minerals, however,
526 counteracts this process by opening new pathways for fluid circulation, thereby enhancing
527 permeability. Intermediate clay-rich facies that would complete the data set between PA10.1
528 and PA11 would be needed to increase the robustness of the relationship observed.

529 Unfortunately, such samples were not recognized at the investigated scale due to the
530 sharpness of the transition between very altered to poorly altered zones.

531 *4.5 Impact of argillic alteration on the electrical conductivity*

532 Figure 8 shows the variation in bulk conductivity measured for each sample depending
533 on the electrical conductivity of the saturating fluid on a log-log scale. For all samples, the
534 bulk conductivity increases with increasing electrical conductivity and presents the typical
535 evolution observed for argillized rocks containing clay minerals with a significant cation
536 exchange capacity (CEC) (Revil et al. 2002; Flóvenz et al. 2005; Komori et al. 2010). Indeed,
537 the electrical conduction in saturated rocks typically involves two different mechanisms:
538 electrolytic conduction, related to the migration of cations and anions through the connected
539 pore space, and surface conduction, enabled by the presence of high-CEC minerals (e.g.,
540 smectite), present at the surface as weakly adsorbed cations. The latter mechanism is
541 generally justified through the formation of an electrical double layer at the mineral surface
542 when put in contact with an electrolyte (Gouy 1910; Chapman 1913 and Stern 1924). Both
543 mechanisms are represented in Figure 8. At a low solution conductivity (from 200 to ~2000
544 $\mu S\ cm^{-1}$), surface conduction is the dominant electrical conduction mechanism and results in
545 the apparent flat part of the plot, especially notable for the PA 12 sample, while at a higher
546 solution conductivity (from ~10,000 to 30,000 $\mu S\ cm^{-1}$), electrolytic conduction dominates,
547 resulting in the linear increasing trend (log-log scale) observed.

548 As expected, the two most argillized samples (i.e., PA12 and PA11) have significantly
549 higher bulk electrical conductivities than the rest of the samples due to the higher abundances
550 of montmorillonite. However, the PA 10.1 sample, which was considered to be moderately
551 argillized (clay mineral abundance: 8.09 %), exhibited an excess electrical conductivity. From
552 the QEMSCAN® analysis, a strong association of montmorillonite with sulphide minerals
553 was observed, unique among the samples investigated. If these sulphide minerals constitute a

554 connected network, they could be the reason for the high electrical conductivity. A third
555 mechanism of electrical conduction could therefore be involved in the PA 10.1 sample
556 corresponding to electronic conduction, in which the charge carriers are the valence electrons
557 located in the outer shell of metallic atoms.

558 In the area of Petite-Anse, the magnetotelluric survey performed during the 2012-2013
559 exploration phase by Coppo et al. (2014) revealed electrical resistivities < 10 Ohm.m at
560 shallow depths. This value is very similar to the electrical resistivities measured in this work
561 for the most argillized samples PA11 and PA12 exhibiting resistivities (after conversion from
562 conductivities) ranging from 9.6 to 1.8 Ohm.m and from 8.0 to 2.7 Ohm.m, respectively,
563 which are in the range of the saturating solution salinities used.

564 In Figure 9 (A), the bulk conductivities of the samples saturated with the 2 wt % NaCl
565 solution are plotted against the structural water proportions and methylene blue values (A and
566 B, respectively). An increasing trend is observed between the bulk conductivities and
567 structural water proportions with a relatively good correlation (R^2= 0.8591), as expected from
568 the increasing contribution of the surface conductivity resulting from the increasing
569 montmorillonite abundances. From this figure, it seems nevertheless difficult to discriminate
570 the samples with low H2O+ values (low clay mineral abundances). A better correlation
571 coefficient is found (R^2= 0.9579) when the electrical conductivities are plotted against the
572 methylene blue values (Figure 9, B). This results from the fact that the methylene blue value
573 is mainly representative of the clay mineral abundance with a high CEC. On the other hand,
574 structural water proportion measurement integrates the kaolinite abundance, a clay mineral
575 known to have a low CEC and therefore contributes to a limited extent to electrical
576 conduction, hence the lower correlation coefficient.

577 Several indicators have been used in the literature to evaluate the contribution of the
578 surface conductivity arising from clay minerals, especially smectite. The surface or interface

conductivity is generally derived from electrical conductivity models, such as the one of Waxman and Smits (1968) or more recently, the one of Revil and Glover (1998). In this work, to evaluate the contribution of surface conductivity, we used the isoconductivity point, as defined by Shainberg et al. (1980) corresponding to the conductivity value for each sample where its bulk conductivity and solution conductivity are equal.

Figure 10 presents the plot of this indicator against the methylene blue value. As shown in Figure 13, we were able to determine the isoconductivity point only for 5 samples (i.e., PA 3.2, PA 5.1 PA 10.1 PA 12 and PA 11) due to the low bulk conductivities of the remaining samples. A strong and linear correlation is found (R^2= 0.9806) between the isoconductivity point and methylene blue value, revealing the strong relation between this indicator and the abundance of montmorillonite.

5. Conclusion

In this work, the evolution of the petrophysical properties (i.e., connected porosity, permeability and electrical conductivity) of the samples collected at the Petite Anse-Diamant hydrothermal system was investigated on the basis of the quantitative evaluation of minerals by scanning electron microscopy (QEMSCAN®) method. The crystal lattice water abundance was found to be a relevant indicator of the clay mineral abundance for the sample series. From the ^{14}C-PMMA autoradiograph analysis, the development of argillic alteration, sometimes superimposed by weathering alteration (i.e., PA 11), leads to an increase in the connected porosity, primarily due to the replacement of the rock matrix and pre-existing minerals by clay minerals, identified here as montmorillonite and kaolinite. Dissolution vugs and fracturing were found to be significant in several samples and contribute to the increases in connected porosities observed. The crystallization of silica, iron oxides and carbonates counteracts this process, leading to a decrease in the connected porosity. The permeability measurements revealed a significant decrease of 2 to 4 orders of magnitude when compared to

604 the permeability data acquired for andesites in the literature. No clear relation to the increase
605 in clay mineral abundance was observed; however, the low permeabilities classically
606 observed for rocks belonging to the caprock formation should be reached during the first steps
607 of argillic alteration development. The electrical conductivity measured for the whole sample
608 series shows a linear relationship with the montmorillonite abundance, represented in this
609 work by the methylene blue value, which is easy to acquire in the laboratory and in the field.

610 Consequently, these new data obtained by coupling different techniques provide three
611 results in a practical and modeling viewpoint. First, they confirm the interest of using
612 geophysical methods based on resistivity measurement (e.g., Direct Current resistivity method
613 and low-frequency electromagnetic methods) to locate caprock formations especially rich in
614 montmorillonite. Let us recall that these geophysical techniques referred as electrical methods
615 share the advantages of being fast, non-intrusive and covering wide areas of investigation in
616 comparison with conventional methods (e.g., drilling, field sampling). Second, our data show
617 that there exist no clear relationship between permeability and clay abundance and thus
618 between permeability and electrical resistivity. Consequently, there is little hope to
619 characterize quantitatively in the field the hydraulic properties of caprock formations by
620 electrical methods. Third, the combination of mineral maps and spatial distribution of the
621 connected porosity observed in autoradiographs allows to clearly discriminate two types of
622 porosity existing in caprock formations: porosity associated with clay mineral phases and that
623 related to dissolution vugs and fractures. Thus our approach provides a quantitative
624 petrographycal basis for modeling the hydraulic properties of caprock formations considered
625 as dual-porosity systems.

626 This work suggests the need for further investigations in two directions. First, this
627 work has accounted for classical petrophysical properties (bulk connected porosity,
628 permeability and electrical conductivity), but recent studies carried out in similar contexts

have shown the possibility of using new non-intrusive indicators based on low-frequency electromagnetic measurements (e.g., the quadrature conductivity and the normalized chargeability; see Revil et al., 2017; Ghorbani et al., 2018; Lévy et al., 2019). These new indicators can be useful in supplementing the information provided by conventional electrical resistivity measurements and should also be compared to mineralogical and petrographic data. Second, the methodology used in this work based on the coupling of innovative techniques (mineral mapping, ^{14}C-PMMA method and petrophysical properties) could be applied to investigate the impact of HT hydrothermal alteration (200-300°C) located at the reservoir level of high-enthalpy hydrothermal systems. These studies would clearly require an adaptation of the experimental conditions through measurement of the same properties as a function of the temperature and pressure.

Acknowledgements: The authors are grateful to Juuso Sammaljärvi, Eveliina Muuri and Marja Siitari-Kauppi for the fruitful discussions on the ^{14}C-PMMA method and for the preparation of the samples. This work was partly carried out with the financial support of the ANR Agence Nationale de la Recherche (French National Research Agency), project ANR-17-CE06-0012-03 ExCiTING (Exploration des ressources géologiques et des reservoirs par prospection géophysique des propriétés des argiles). The authors also acknowledge financial support from the European Union (ERDF) and Région Nouvelle Aquitaine. We would like to thank Kristian Bär and Jamie Farquharson for their thorough review which helped us improve the manuscript.

Appendix A. Supplementary data. QEMSCAN® maps.

References

654 Ahmed, A. S., Revil, A., Byrdina, S., Coperey, A., Gailler, L., Grobbe, N., Viveiros F., Silva
655 C., Jougnot D., Ghorbani A., Hogg, C., Kiyan D., Rath V., Heap M.J., Grandis H.,
656 Humaida H., 2018. 3D electrical conductivity tomography of volcanoes. J. of Volcanol.
657 Geotherm. Res. 356, 243-263.
658 Archie, G.E., 1942. The electrical resistivity log as an aid in determining some reservoir
659 characteristics. Transactions of the AIME 146 (01): 54–62.
660 Arnason, K., Karlsdottir, R., Eysteinsson, H., Flóvenz, O.G., Gudlaugsson, S.T., 1992. The
661 resistivity structure of high-temperature geothermal systems in Iceland. In: E. Iglesias, D.
662 Blackwell, T. Hunt, J. Lund and S. Tamanyu (Eds.), Proceedings of the World Geothermal
663 Congress 2000, Kyushu-Tohoku, Japan, 923–28.
664 Avellaneda, M. Torquato, S., 1991. Rigorous link between fluid permeability, electrical
665 conductivity, and relaxation times for transport in porous media. Physics of Fluids A: Fluid
666 Dynamics 3 (11): 2529–40.
667 Ayling, B., Rose, P., Petty, S., Zemach, E., Drakos, P., 2012. QEMSCAN (Quantitative
668 Evaluation of Minerals by Scanning Electron Microscopy): Capability and application to
669 fracture characterization in geothermal systems. Proceedings of the Thirty-Seventh
670 Workshop on Geothermal Reservoir Engineering. Stanford, California: Stanford
671 University, January 30 - February 1, 2012.
672 Beaufort, D., Patrier, P., Meunier, A. Ottaviani M.M., 1992. Chemical variations in
673 assemblages including epidote and/or chlorite in the fossil hydrothermal system of Saint
674 Martin (Lesser Antilles). J. Volcanol. Geotherm. Res. 51, 95–114.
675 https://doi.org/10.1016/0377-0273(92)90062-I.
676 Bernard, M.L., Zamora, M., Géraud, Y., Boudon, G, 2007. Transport Properties of Pyroclastic
677 Rocks from Montagne Pelée Volcano (Martinique, Lesser Antilles). J. Geophys. Res., 112
678 (B5).

679 Björbsson, G., Bodvarsson, G., 1990. A survey of geothermal reservoir properties.
680 Geothermics. 19, 17–27.
681 Boitnott, G.N., Boyd, P.J., 1996. Permeability, electrical impedance, and acoustic velocities
682 on reservoir rocks from the Geysers geothermal field. Proceedings of the Twenty-First
683 Workshop on Geothermal Reservoir Engineering. Stanford University, Stanford,
684 California. January 22-24. 1996.
685 Bonnet, M., Sardini, P., Billon, S., Siitari-Kauppi, M., Kuva, J., Fonteneau, L., Caner, L.
686 2020. Determining crack aperture distribution in rocks using the 14C-PMMA
687 autoradiographic method: experiments and simulations. J. Geophys. Res., 125,
688 e2019JB018241.
689 Bouysse, P., Westercamp, D., 1990. Subduction of atlantic aseismic ridges and late Cenozoic
690 evolution of the Lesser Antilles Island Arc. Tectonophysics. 175, 349357–380.
691 Browne, P.R.L., 1978. Hydrothermal alteration in active geothermal fields. Ann Rev. of Earth
692 and Planetary Sci. 6, 229–48.
693 Cai, J., Wei, W., Hu, X., Wood, DA., 2017. Electrical conductivity models in saturated
694 porous media: a review. Earth Sci. Rev. 171, 419–33.
695 Caldwell, G., Pearson, C. Zayadi, H. 1986. Resistivity of rocks in geothermal systems: a
696 laboratory study. In proceedings 8th NZ geothermal workshop, 227–31.
697 Chapman, D.L., 1913. LI. A Contribution to the Theory of Electrocapillarity. The London,
698 Edinburgh, and Dublin Philosophical Magazine and Journal of Science 25 (148): 475–81.
699 Coppo, N., Baltassat, J.M., Girard, J.F., Jacob, T., Martelet, G., Mathieu, F. and Wawrzyniak,
700 P., 2014. Exploration géophysique (magnétotellurique et gravimétrie) du potentiel
701 géothermique de La Martinique (Montagne Pelée, Anses d'Arlet, Pitons Du Carbet et
702 Lamentin). Final report (in French). RP-62745-FR. BRGM. 278.

703 Cormy, G., Demians d'Archimbaud, J., Surcin, J., 1970. Prospection géothermique aux
704 Antilles Françaises, Guadeloupe et Martinique. Geothermics. 2, 57–72.
705 Cosenza, P., Ghorbani, A., Florsch, N., Revil, A. 2007. Effects of drying on the low-
706 frequency electrical properties of Tournemire argillites. Pure Appl. Geophys. 164, 2043-
707 2066.
708 De Maisonneuve, C.B., Bachmann, O. and Burgisser, A., 2009. Characterization of juvenile
709 pyroclasts from the Kos Plateau Tuff (Aegean Arc): insights into the eruptive dynamics of
710 a large rhyolitic eruption. Bul. Volcanol. 71, 643.
711 Degruyter, W., Bachmann, O. and Burgisser, A., 2010. Controls on magma permeability in
712 the volcanic conduit during the climactic phase of the Kos Plateau Tuff eruption (Aegean
713 Arc). Bul. Volcanol. 72, .63.
714 Delayre C. 2018. Couplages altérations hydrothermales du caprock / propriétés
715 pétrophysiques des roches en contexte géothermal de haute enthalpie. PhD thesis,
716 University of Poitiers (France) (in French).
717 Dobson, P.F., Kneafsey, T.J., Hulen, J., Simmons, A., 2003. Porosity, permeability, and fluid
718 flow in the Yellowstone geothermal system, Wyoming. J. Volcanol. Geotherm. Res. 123,
719 313–24.
720 Escobedo, D., 2018. Study of hydrothermal alteration and petrophysical properties of well
721 KH6 Krafla geothermal field, NE Iceland. Internship Geosciences Montpellier, 60p.
722 Farquharson, J., Heap, M.J., Varley, N.R., Baud, P. and Reuschlé, T., 2015. Permeability and
723 porosity relationships of edifice-forming andesites: a combined field and laboratory study.
724 J. Volcanol. Geotherm. Res. 297, 52-68.
725 Flóvenz, ÓG., Spangenberg, E., Kulenkampff, J., Árnason, K., Karlsdóttir, R. Huenges, E.,
726 2005. The role of electrical interface conduction in geothermal exploration. Proceedings
727 World Geothermal Congress 2005, Antalya, Turkey, 24-29 April 2005, 24–29.

728 Franklin, J.A., Vogler U.W., Szlavin, J., Edmond, J.M. Z.T. Bieniawski. 1981. Suggested
729 methods for the determining water content, porosity, density, absorption and related
730 properties and swelling and slake-durability index properties. In ISRM Suggested
731 Methods: Rock Characterisation, Testing and Monitoring, Pergamon Press.
732 Frolova, J., Ladygin, V. Rychagov, S., 2001. Geothermal reservoir study through
733 petrophysical data. Geothermal Resources Council Transactions. 25, 401–3.
734 Frolova, J., Ladygin, V. Rychagov, S., 2006. Petrophysical properties of argillitization zone in
735 geothermal fields. Geothermal Resource Council Transactions. 30, 909–12.
736 Frolova, J., Gvozdeva, I.P., Kuznetsov, N.P., 2015. Effects of hydrothermal alterations on
737 physical and mechanical properties of rocks in the Geysers Valley (Kamchatka Peninsula)
738 in connection with landslide development. Proceedings World Geothermal Congress 2015
739 Melbourne, Australia, 19-25 April 2015, 1–6.
740 Frolova, J.V., Ladygin, V.M. Rychagov, S.N., 2010. Petrophysical alteration of volcanic
741 Rocks in hydrothermal systems of the Kuril-Kamchatka Island Arc. Proceedings World
742 Geothermal Congress 2010 Bali, Indonesia, 25-29 April 2010.
743 Gadalia, A., Baltassat J.M., Bouchot, V., Caritg, S., Coppo, N., Gal, F., Girard, J.F.,
744 Gutierrez, A., Jacob, T. Martelet, G., 2014. Compléments d'exploration géothermique en
745 Martinique: conclusions et recommandations pour les zones de La Montagne Pelée, des
746 Anses d'Arlet, des Pitons du Carbet et du Lamentin, 2014. Final Report (in French).
747 BRGM/RP-FR 227.
748 Gadalia, A., Baltassat J.M., Bouchot, V., Caritg-Monnot, S., Gal, F., Girard J.F., Gutierrez A.,
749 Jacob T., Martelet G., Coppo N., Rad S., Tailame A.L., Traineau H., Vittecoq B.,
750 Wawrzyniak P., 2015. The Petite Anse-Diamant geothermal system (Martinique Island,
751 Lesser Antilles): Results of the 2012-2013 exploration. Proceedings of World Geothermal
752 Congress 2015. Melbourne, Australia. https://hal-brgm.archives-ouvertes.fr/hal-01102469.

753 Genter, A., Roig, J.Y., 2003. Réévaluation du potentiel géothermique dans les régions de
754 Morne Rouge - Montagne Pelée et du Diamant (Martinique): Étude Géologique. Report
755 RP-52546-FR. BRGM (in French).
756 Gerber, L., Maréchal, F., 2012. Environomic optimal configurations of geothermal energy
757 conversion systems: application to the future construction of enhanced geothermal systems
758 in Switzerland. Energy, 45, 908–23.
759 Germa, A., Quidelleur X., Labanieh S., Chauvel C., Lahitte, P., 2011. The volcanic evolution
760 of Martinique Island: insights from K–Ar dating into the Lesser Antilles Arc migration
761 since the Oligocene. J. Volcanol. Geotherm. Res. 208, 122–35.
762 Gonzales, K., Finizola, A., Lénat, J.F., Macedo, O., Ramos, D., Thouret, J.C., Fournier, N.,
763 Cruz, V. Pistre, K., 2014. Asymmetrical structure, hydrothermal system and edifice
764 stability: the case of Ubinas volcano, Peru, revealed by geophysical surveys. J. Volcanol.
765 Geotherm. Res. 276: 132–44.
766 Ghorbani, A., Revil, A., Coperey, A., Ahmed, A. S., Roque, S., Heap, M. J., Grandis H.
767 Viveiros, F. 2018. Complex conductivity of volcanic rocks and the geophysical mapping of
768 alteration in volcanoes. J. Volcanol. Geotherm. Res. 357, 106-127.
769 Gouy, M. 1910. Sur la constitution de la charge électrique à la surface d'un électrolyte. J.
770 Phys. Theor. Appl. 9 (1): 457–68.
771 Hang, P.T. Brindley, G.W., 1970. Methylene blue absorption by clay minerals. Determination
772 of surface areas and cation exchange capacities (clay-organic studies XVIII). Clays Clay
773 Min. 18, 203–12.
774 Heap, M.J. and Kennedy, B.M. 2016. Exploring the scale-dependent permeability of fractured
775 andesite. Earth Planet. Sci. Lett. 447,139–150.
776 Heap, M.J., Kennedy, B.M., Farquharson, J.I., Ashworth, J., Mayer, K., Letham-Brake, M.,
777 Reuschlé, T., Gilg, H.A., Scheu, B., Lavallée, Y. and Siratovich, P., 2017. A

778 multidisciplinary approach to quantify the permeability of the Whakaari/White Island
779 volcanic hydrothermal system (Taupo Volcanic Zone, New Zealand). J. Volcanol.
780 Geotherm. Res. 332, 88-108.
781 Heap, M.J., Troll, V.R., Kushnir, A.R., Gilg, H.A., Collinson, A.S., Deegan, F.M.,
782 Darmawan, H., Seraphine, N., Neuberg, J. and Walter, T.R., 2019. Hydrothermal alteration
783 of andesitic lava domes can lead to explosive volcanic behaviour. Nature com. 10, 1-10.
784 Heap, M.J., Gravley, D.M., Kennedy, B.M., Gilg, H.A., Bertolett, E. and Barker, S.L., 2020.
785 Quantifying the role of hydrothermal alteration in creating geothermal and epithermal
786 mineral resources: the Ohakuri ignimbrite (Taupō Volcanic Zone, New Zealand). J.
787 Volcanol. Geotherm. Res., https://doi.org/10.1016/j.jvolgeores.2019.106703.
788 Hellmuth, K.H., Siitari-Kauppi, M., 1990. Investigation of the porosity of rocks: impregnation
789 with ^{14}C-Polymethylmethacrylate (PMMA), a new technique. Helsinki: Finnish Centre for
790 Radiation and Nuclear Safety : Finnish Government Printing Centre. ISBN 9517-3949-3.
791 Hellmuth, K.H., Siitari-Kauppi M. Lindberg A., 1993. Study of porosity and migration
792 pathways in crystalline rock by impregnation with 14C-Polymethylmethacrylate. J.
793 Contaminant Hydrol. 13, 403–18. https://doi.org/10.1016/0169-7722(93)90073-2.
794 Henley, R.W. Ellis, A.J., 1983. Geothermal systems ancient and modern: a geochemical
795 review. Earth Sci. Rev. 19, 1–50.
796 Hughes, J.C., 1980. Crystallinity of kaolin minerals and their weathering sequence in some
797 soils from Nigeria, Brazil and Colombia. Geoderma 24, 317–25.
798 https://doi.org/10.1016/0016-7061(80)90059-2.
799 Inoue, A. 1995. Formation of Clay Minerals in Hydrothermal Environments. In: B. Velde
800 (Ed.), Origin and Mineralogy of Clays, 268–329. Berlin, Heidelberg: Springer Berlin
801 Heidelberg. https://doi.org/10.1007/978-3-662-12648-6_7.

802 Jayawardena, U.S. Izawa, E., 1994a. Application of present indices of chemical weathering
803 for Precambrian metamorphic rocks in Sri Lanka. Définition d'indices d'altération pour
804 des roches métamorphiques Précambriennes, Sri Lanka. Bull. Int. Ass. Eng. Geol. 49, 55.
805 Jayawardena, U.S. Izawa, E., 1994b. A new chemical index of weathering for metamorphic
806 silicate rocks in tropical regions: a study from Sri Lanka. Eng. Geol., 36, 303–10.
807 Kagel, A. Gawell, K., 2005. Promoting geothermal energy: air emissions comparison and
808 externality analysis. The Electricity J., 18, 90–99.
809 Kahr, G., Madsen, F.T., 1995. Determination of the cation exchange capacity and the surface
810 area of bentonite, illite and kaolinite by methylene blue adsorption. Appl. Clay Sci. 9, 327–
811 36.
812 Kanaya, K., Okayama, S., 1972. Penetration and energy-loss theory of electrons in solid
813 targets." J. Phys. D: Appl. Phys. 5, 43.
814 Komori, S., Kagiyama, T., Hoshizumi, H., Takakura, S., Mimura, M., 2010. Vertical mapping
815 of hydrothermal fluids and alteration from bulk conductivity: simple interpretation on the
816 USDP-1 Site, Unzen Volcano, SW Japan. J. Volcanol. Geotherm. Res. 198, 339–47.
817 Kristinsdóttir, L.H., Flóvenz, Ó.G., Árnason, K., Bruhn, D., Milsch, H., Spangenberg, E.
818 Kulenkampff, J., 2010. Electrical conductivity and P-Wave velocity in rock samples from
819 high-temperature icelandic geothermal fields. Geothermics. 39, 94–105.
820 Lévy, L., Gibert, B. Sigmundsson, F. Flóvenz, Ó. G. Hersir, G. P. Briole, P., Pezard, P. A.
821 2018. The role of smectites in the electrical conductivity of active hydrothermal systems:
822 electrical properties of core samples from Krafla volcano, Iceland. Geophys. J. Intern. 215,
823 1558-1582.
824 Lévy, L., Maurya, P. K., Byrdina, S., Vandemeulebrouck, J., Sigmundsson, F., Arnason, K.,
825 Ricci T., Deldicque D., Roger M., Gibert, B., Labazuy, P. 2019. Electrical resistivity
826 tomography and time-domain induced polarization field investigations of geothermal areas

827 at Krafla, Iceland: comparison to borehole and laboratory frequency-domain electrical
828 observations. Geophys. J. Intern. 218, 1469-1489.
829 Lorenz, P.M. 1999. Determination of the cation exchange capacity (CEC) of clay minerals
830 using the complexes of copper (II) ion with triethylenetetramine and
831 tetraethylenepentamine. Clays Clay Miner. 47, 386–88.
832 Macdonald, R., Hawkesworth, C.J., Heath, E., 2000. The Lesser Antilles volcanic chain: a
833 study in arc magmatism. Earth Sci. Rev. 49, 1–76. https://doi.org/10.1016/S0012-
834 8252(99)00069-0.
835 Mayer, K., Scheu, B., Montanaro, C., Yilmaz, T.I, Isaia, R., Aßbichler, D. Dingwell, D.B.,
836 2016. Hydrothermal alteration of surficial rocks at Solfatara (Campi Flegrei): petrophysical
837 properties and implications for phreatic eruption processes J. Volcanol. Geotherm. Res.
838 320, 128–43.
839 Mazurier, A., Sardini, P., Rossi, A. M., Graham, R. C., Hellmuth, K. H., Parneix, J. C.,
840 Sitaari-Kaupi, M., Voutilainen, M., Caner, L. 2016. Development of a fracture network in
841 crystalline rocks during weathering: Study of Bishop Creek chronosequence using X-ray
842 computed tomography and 14C-PMMA impregnation method. GSA Bul., 128(9-10),
843 1423-1438.
844 Meunier, A., Beaufort, D., 2017. Clay minerals in hydrothermal systems. Geochimica
845 Brasiliensis 10, 347–63.
846 Mielke, P, Prieto, A.M., Bignall, G. Sass, I., 2015. Effect of hydrothermal alteration on rock
847 properties in the Tauhara Geothermal Field, New Zealand. Proceedings World Geothermal
848 Congress 2015 Melbourne, Australia, 19-25 April 2015.
849 Milsch, H., Blöcher, G., Engelmann, S., 2008. The relationship between hydraulic and
850 electrical transport properties in sandstones: An experimental evaluation of several scaling
851 models. Earth Planet. Sci. Lett. 275, 355–63.

852 Mordensky, S.P., Villeneuve, M.C., Kennedy, B.M., Heap, M.J., Gravley, D.M., Farquharson,
853 J.I., Reushlé, T. 2018. Physical and mechanical property relationships of a shallow
854 intrusion and volcanic host rock, Pinnacle Ridge, Mt. Ruapehu, New Zealand. J. Volcanol.
855 Geotherm. Res. 359, 1–20.
856 Mordensky, S.P., Kennedy, B.M., Villeneuve, M.C., Lavallée, Y., Reichow, M.K., Wallace,
857 P.A., Siratovich, P.A. and Gravley, D.M., 2019. Increasing the permeability of
858 hydrothermally altered andesite by transitory heating. Geochem. Geophys. Geosys. 20,
859 5251-5269.
860 Muñoz, G. 2014. Exploring for geothermal resources with electromagnetic methods. Surv.
861 Geophys. 35, 101–22. https://doi.org/10.1007/s10712-013-9236-0.
862 Navelot, V., Géraud, Y., Favier, A., Diraison, M., Corsini, M., Lardeaux, J. M., Verati C,
863 Mercier de Lépinay J. Legendre L., .Beauchamps, G. 2018. Petrophysical properties of
864 volcanic rocks and impacts of hydrothermal alteration in the Guadeloupe Archipelago
865 (West Indies). J. Volcanol. Geotherm. Res. 360, 1-21.
866 Nielson, D. L., Clemente, W. C., Moore, J. N., Powell, T. S. 1996. Fracture permeability in
867 the Matalibong-25 corehole, Tiwi geothermal field, Philippines (No. SGP-TR-151-30).
868 Earth Sciences and Resources Institute, University of Utah, Salt Lake City, UT; Philippine
869 Geothermal, Inc., Metro Manila, PH; Unoal Energy Resouces Division, Santa Rosa, CA.
870 Nehler, M., Andolfsson, T., Stöckhert, F., Renner, J., Bracke, R. 2016. Monitoring fluid-rock
871 interactions at In-Situ conditions using computed tomography. In *Proceedings, 41st*
872 *Workshop on Geothermal Reservoir Engineering, Stanford University, Stanford,*
873 *California, 22–24th 2010, SGP-TR-209*.
874 O'Sullivan, M.J., Pruess, K. Lippmann, M.J., 2001. State of the art of geothermal reservoir
875 simulation. Geothermics. 30, 395–429.

876 Patrier, P., Papapanagiotou, P., Beaufort, D., Traineau, H., Bril, H., and Rojas, J., 1996. Role
877 of permeability versus temperature in the distribution of the fine (< 0.2 Mm) clay fraction
878 in the Chipilapa geothermal system (El Salvador, Central America). J. Volcanol.
879 Geotherm. Res. 72, 101–20. https://doi.org/10.1016/0377-0273(95)00078-X.
880 Petrov, V.A., Poluektov, V.V., Zharikov, A.V., Velichkin, V.I., Nasimov, R.M., Diaur,
881 N.I., Terentiev, V.A., Shmonov, V.M., Vitovtova, V.M. 2005. Deformation of
882 metavolcanics in the Karachay Lake area, Southern Urals: petrophysical and mineral—
883 chemical aspects. In P.K. Harvey, P.A. Pezard, T.S. Brewer, V.A. Petrov (eds).
884 Petrophysical properties of crystalline rock. Geological Society special publication 20.
885 https://doi.org/10.1144/GSL.SP.2005.240.01.22.
886 Pirajno, F., 2009. Hydrothermal processes associated with meteorite impacts. In
887 Hydrothermal Processes and Mineral Systems, 1097–1130. Springer.
888 Pirrie, D., Butcher, A.R., Power, M.R., Gottlieb, P. Miller, G.L., 2004. Rapid quantitative
889 mineral and phase analysis using automated scanning electron microscopy (QemSCAN);
890 potential applications in forensic geoscience." Geological Society, London, Special
891 Publications 232 (1): 123–36. https://doi.org/10.1144/GSL.SP.2004.232.01.12.
892 Pola, A., Crosta, G., Fusi, N., Barberini, V., Norini, G. 2012. Influence of alteration on
893 physical properties of volcanic rocks. Tectonophys. *566*, 67-86.
894 Pola, A., Crosta, G. B., Fusi, N., Castellanza, R., 2014. General characterization of the
895 mechanical behaviour of different volcanic rocks with respect to alteration. Eng. Geol. 169,
896 1-13.
897 Pola, A., Martínez-Martínez, J., Macías, J. L., Fusi, N., Crosta, G., Garduño-Monroy, V. H.,
898 Núñez-Hurtado, J. A. 2016. Geomechanical characterization of the Miocene Cuitzeo
899 ignimbrites, Michoacán, Central Mexico. Eng. Geol. 214, 79-93.

900 Pruess, K., 1990. Modeling of geothermal reservoirs: fundamental processes, computer
901 simulation and field applications. Geothermics. 19, 3–15.
902 Revil, A. Glover P.W.J., 1998. Nature of Surface Electrical Conductivity in Natural Sands,
903 Sandstones, and Clays. Geophys. Res. Lett. 25, 691–94.
904 Revil, A, Hermitte, D., Spangenberg, E. Cochémé, J.J., 2002. Electrical properties of
905 zeolitized volcaniclastic materials. J. Geophys. Res.: Solid Earth, 107 (B8).
906 Revil, A., Murugesu, M., Prasad, M., Le Breton, M. 2017. Alteration of volcanic rocks: A
907 new non-intrusive indicator based on induced polarization measurements. J. Volcanol.
908 Geotherm. Res. 341, 351-362.
909 Revil, A., Qi, Y., Ghorbani, A., Ahmed, A. S., Ricci, T., Labazuy, P. 2018a. Electrical
910 conductivity and induced polarization investigations at Krafla volcano, Iceland. J.
911 Volcanol. Geotherm. Res. 368, 73-90.
912 Revil, A., Ghorbani, A., Gailler, L. S., Gresse, M., Cluzel, N., Panwar, N., Sharma, R. 2018b.
913 Electrical conductivity and induced polarization investigations at Kilauea volcano, Hawai'i.
914 J. Volcanol. Geotherm. Res. 368, 31-50.
915 Roberson, H.E., Lahann, R.W., 1981. Smectite to illite conversion rates: effects of solution
916 chemistry. Clays Clay Min. 29, 129–35.
917 Rybach, L. 2010. The future of geothermal energy and its challenges. Proceedings World
918 Geothermal Congress 2010 Bali, Indonesia, 25-29 April 2010.
919 Sammartino, S., Partier, P., Sardini, P., Meunier, A., Tevissen, E., 1999. Evolution of fluid
920 pathways of Charroux-Civary Tonalite (Part I): alteration effects—an analytical approach.
921 Phys. Chem. Earth, Part A: Solid Earth and Geodesy. 24, 601–6.
922 Sanjuan, B., Romain, M., Michel, B., Foucher, J.C., Roig, J.Y., Baltassat, J.M., 2005.
923 Geothermal exploration in the Mount Pelée volcano-Morne Rouge and Diamant areas

(Martinique, West French Indies): geochemical data. Proceedings World Geothermal Congress 2005 Antalya, Turkey, 24-29 April 2005.

Santamarina, J.C., Klein, K.A., Wang, Y.H., Prencke, E., 2002. Specific surface: determination and relevance. Canadian Geotech. J. 39, 233–41.

Sardini, P., B. Ledésert, G. Touchard, Quantification of microscopic networks by image analysis and measurement of the permeability of the Soultz-sous-Forêts granite (Alsace, France*). Conference Volume of the 9th Kongsberg Seminar, Fluid Flow and Transport in Rocks*, 3-5 mai 1995, Chapman et al. (B. Jamtveit & B. Yardley eds), pp. 171-189, 1996.

Shainberg, I., Rhoades, J.D., Prather, R.J., 1980. Effect of exchangeable sodium percentage, cation exchange capacity, and soil solution concentration on soil electrical conductivity. Soil Sci. Soc. Am. J. 44, 469–73.

Siitari-Kauppi, M., 2002. Development of ^{14}C-Polymethylmethacrylate method for the characterisation of low porosity media. Application to rocks in geological barriers of nuclear waste storage. Ph. D. Thesis of the University of Poitiers (France) and the University of Helsinki (Finland).

Stern, O., 1924. Zur theorie der elektrolytischen doppelschicht. Berichte Der Bunsengesellschaft Für Physikalische Chemie. 30, 508–16.

Stimac, J.A., Powell, T.S., Golla, G.U., 2004. Porosity and permeability of the Tiwi geothermal field, Philippines, based on continuous and spot core measurements. Geothermics. 33, 87–107.

Tester, J.W., Anderson B.J., Batchelor, A.S., Blackwell, D.D., DiPippo, R., Drake, E., Garnish, J., Livesay, B., Moore, M.C., Nichols, K., 2006. The future of geothermal energy. Impact of Enhanced Geothermal Systems (EGS) on the United States in the 21st Century. Massachusetts Institute of Technology, Cambridge, MA, 372.

948 Traineau, H, Bouchot, V., Caritg, S., Gadalia, A., 2013. Compléments d'exploration
949 géothermique en Martinique: volet géologie, Rapport Intermédiaire. BRGM/RP-62349-FR.
950 BRGM (in French).
951 Udagedara, D.T., Oguchi C.T. Gunatilake, J.K., 2017. Evaluation of geomechanical and
952 geochemical properties in weathered metamorphic rocks in tropical environment: a case
953 study from Samanalawewa hydropower project, Sri Lanka. Geosci. J. 21, 441–52.
954 Ussher, G., Harvey, C., Johnstone, R., Anderson, E., 2000. Understanding the resistivities
955 observed in geothermal systems. Proceedings World Geothermal Congress 2000 Kyushu -
956 Tohoku, Japan, May 28 - June 10, 2000.
957 Waxman, M.H., Smits, L.J.M., 1968. Electrical conductivities in oil-bearing shaly sands. Soc.
958 Petrol. Eng. J. 8, 107–22.
959 White, N.C., Hedenquist, J.W., 1990. Epithermal environments and styles of mineralization:
960 variations and their causes, and guidelines for exploration. J. Geochem. Explor. 36, 445–
961 74.
962 Wollentz, K.and Heiken, G. 1992. Volcanology and geothermal energy. Univ. of California
963 press. http://ark.cdlib.org/ark:/13030/ft6v19p151/.
964 Wright, H.M.N., Cashman, K.V., Gottesfeld, E.H., Roberts, J.J, 2009. Pore structure of
965 volcanic clasts: measurements of permeability and electrical conductivity. Earth Planet.
966 Sci. Lett. 280, 93–104.
967 Wyering, L.D., Villeneuve, M. Wallis, I., 2012. The effects of hydrothermal alteration on
968 mechanical rock properties of the Andesite Breccia and Tahorakuri Formation from the
969 Ngatamariki geothermal field, New Zealand and empirical relations between rock strength
970 and physical properties. Proceedings of New Zealand geothermal workshop, Auckland,
971 New Zealand (34). https://www. geothermal-library. org. 2012.

Wyering, L.D., Villeneuve, M.C., Wallis, I.C., Siratovich, P.A., Kennedy, B.M., Gravley, D.M. and Cant, J.L., 2014. Mechanical and physical properties of hydrothermally altered rocks, Taupo volcanic zone, New Zealand. J. Volcanol. Geotherm. Res. 288, 76–93.

Yukselen, Y., and Kaya, A., 2008. Suitability of the methylene blue test for surface area, cation exchange capacity and swell potential determination of clayey soils. Eng.Geol. 102, 38–45.

Figure captions

Figure 1: Locations of the Petite Anse-Diamant area on Martinique Island (A) and the samples investigated in this study (B). The red point (E-F) indicates the location of the Eaux-Ferrées thermal source (source: IGN, French institute of geography).

Figure 2: (A) Experimental setup for the permeability measurements (Sammartino et al. 1999). (B) Cross-section of the permeability cell with (1) the pressure vessels of stainless steel, (2) the confining cell and (3) the plug sample. (C) Perspective view of the plug sample with the diameters of the core sample and plug opening (mm).

Figure 3: Resistivity cell used for acquisition of the impedance spectra.

Figure 4: QEMSCAN® mineral maps of samples PA13.2, PA13.1, PA4, PA 7.2, PA10.1, PA12 and PA 11. White areas are pixels detected as porosity. Sample PA13 is the freshest sample of andesite, presenting moderate alteration of hornblende to montmorillonite at the bottom of the section (arrow 3), and silica and oxides abundance in the mesostase (arrows 1 and 2). In sample PA4, intragranular alteration of hornblende crystals is underscored by montmorillonite and oxides in cleavage planes. Sample PA10.1 exhibits pervasive alteration of the mesostase (presence of montmorillonite, silica, and sulphide minerals) (arrows 1,2). In sample PA12, hornblende crystals are totally replaced by montmorillonite and iron oxides (arrow 1); carbonate veins are also detected (arrow 2). Sample PA11 is extremely altered; hornblende is totally replaced by silica and montmorillonite (arrow 3), and feldspars phenocrysts are partially dissolved, containing dissolution voids(arrow 2), which are partially filled with kaolinite and silica (arrow 1). In this sample, quartz grains remains unaltered.

Figure 5: Correlation plot between the abundances of the clay phases identified by the QEMSCAN® system and the crystal lattice water proportions obtained from bulk-rock chemical analysis. Mt = montmorillonite and K = kaolinite.

1003 Figure 6: QEMSCAN® Mineral maps (left) and related autoradiographs (right) from the ^{14}C-
1004 PMMA method of samples PA 13, PA 4, PA 10.1, PA 12 and PA 11. In autoradiographs, the
1005 darker the grey level is, the higher the porosity is. In the freshest sample (PA13) the most
1006 porous mineral is hornblende, partially replaced by montmorillonite in PA 13.1 side (arrow
1007 1). In PA4 sample, porosity is well developed in hornblende cleavage planes (arrow 1), and
1008 corresponds to montmorillonite; feldspars remains lowly porous (arrow 2). In sample PA
1009 10.1, low porosity area are initial feldspar phenocrysts (arrow 2), but are also in sulphide of
1010 pseudomorphosed hornblende (arrow1) and in carbonate cements. Montmorillonite-rich areas
1011 and in a less extent mesostase present an higher porosity. In PA12, Feldspars remain unaltered
1012 and lowly porous (arrow 1), as well carbonate. High porosity of pseudomorphosed hornblende
1013 cannot be differentiate from the porosity of the mesostase (arrow 3).
1014 Sample PA11, which is the most affected by hydrothermal alteration, presents a totally
1015 different porosity pattern than sample PA12. In this sample, quartz grains remains the only
1016 lowly porous mineral (arrow 3). The connected mesostase matrix is porous, but
1017 pseudomorphosed hornblende (arrow 1) and altered/dissolved feldspars associated with
1018 dissolution voids (arrow 2) are more porous.
1019 Figure 7: (A) Plot of the connected porosity of the samples against the structural water
1020 content (H_2O^+) value obtained with the triple weight (TW) method and from bulk-rock
1021 chemical analysis. The H_2O^+ values are used as indicators of the clay mineral abundances (see
1022 section 2.2). (B) Darcian permeability against the connected porosity.
1023 Figure 8: Bulk conductivities versus conductivities of the solutions saturating the samples.
1024 The 1:1 line is used to estimate the isoconductivity point of each sample.
1025 Figure 9: Correlation plots of the bulk conductivity measured for the samples saturated with
1026 the 2 wt % NaCl solution depending on the structural water proportion (H_2O^+) (A) and blue
1027 methylene (BM) value (B).

Figure 10: Evolution of the isoconductivity point depending on the blue methylene (BM) value.

Table captions

Table 1: Description of color and consolidation of each samples.

Table 2. Comparison of ^{14}C-PMMA porosity method with conventional imaging methods.

Table 3: Quantitative evaluation of rock mineral composition from QEMSCAN® analysis.

Table 4: Crystal lattice water proportions (H_2O^+) from bulk-rock chemical analysis; connected porosities φ_{tw} and φ_{FA} obtained by triple-weighted method (TW) and from film autoradiography (FA) respectively and Darcian permeabilities k of samples.

Table 5. Conductivities of the solutions saturating the samples and bulk conductivities (expressed in $\mu S.cm^{-1}$).

		Consolidation	Color
PA 1		good	grey
PA 2		good	grey
PA 3	PA 3.1	good	grey
	PA 3.2	good	red wall-rock (FeOx)
PA 4		good	grey
PA 5.1		moderate	grey yellowish
PA 7.2		moderate	whitish grey
PA 10.1		good	dark grey
PA 11		poorly consolidated	yellowish
PA 12		poorly consolidated	greenish
PA13	PA 13.1	good	whitish grey
	PA 13.2	very hard	red wall-rock (FeOx)

Table 1: Description of color and consolidation of each samples.

Porosimetric Method	Raw data	Connected/Total	Sample size	Advantages	Drawbacks
14C-PMMA (imaging)	2D porosity map from activity map and calibration	3D Connected	dm3 to > cm3	• Porosity map regardless of pore size. • Pore type distinction. 2D porosity mapping easy to analyse. • Fracture aperture distribution	• Use of radioactive resins. • Adaptation in development for swelling clay samples. • "Confidential" method. • Non applicable to naturally radioactive sample.
XRCT (imaging)	3D map of resolved pores from X-Ray attenuation map	Total and/or 3D connected	dm^3 to mm^3	• 3D mapping of pores. • 3D pore size and geometry. 3D grid/mesh for transport modelling. • Good availability	• Data difficult to handle and complex to process. • Pore resolution depends on voxel size. • Segmentation of pores is often complicated. • Grey levels are not only a function of porosity
SEM - BSE (imaging)	2D map of resolved pores from BSE images	Total	Thin section	• Pore type distinction. • 2D mapping of pores	• Using large mosaic image, Data are heavy to handle. Pore resolution depends on pixel size. • Grey levels levels are not only a function of porosity.
Gas adsorption methods BJH	Pore size distribution	3D Connected	mm^3	• Fast and widely used	• Pore size from 3 to 300 nm. • Not a porosity measurement technique.
Hg-porosimetry	Bulk value and throat size distribution	3D Connected	cm^3	• Fast and widely used	• Not pore size, but throat size. • Toxicity of Hg.

Water porosity by Triple Weighting	Bulk value	3D Connected	dm^3 to mm^3	• Fast and cheap. • Essential for controlling porosity from imaging methods	• Only bulk method. • Speed of water intrusion depend on rock water permeability, and can be long.
He-Pycnometry	bulk value	3D Connected	cm3 to mm3	• Fast intrusion of He. • Cheap. • Essential for controlling porosity from imaging methods	• Only bulk. • Apparent volume should be known to determine porosity.

1059 Table 2. Comparison of ^{14}C-PMMA porosity method with conventional imaging methods.

1060

1061

	PA 13.2	PA 13.1	PA 3.1	PA 10.1	PA 4	PA 7.2	PA 12	PA 11
Mesostasis	32.79	43.71	38.76	38.38	34.85	30.53	40.37	34.57
Andesine	16.87	17.23	20.68	19.27	21.49	20.85	13.81	2.81
Labradorite	12.59	13.64	13.97	10.64	12.92	13.22	5.89	0.24
Oligoclase	5.38	6.98	3.44	2.3	3.07	2.63	3.56	1.22
Bytownite	0.48	0.58	0.59	0.38	0.55	0.62	0.05	-
Hornblende	13.9	4.91	3.43	0.1	4.88	9.82	0.5	0.33
Montmorillonite	4.69	5.35	6.55	7.08	9.57	10.73	15.21	22.74
Kaolinite	0.99	0.69	0.68	1.01	0.94	1.02	3.92	14.82
Quartz/Silica	8.64	4.91	7.87	14.77	8.2	8.54	12.74	21.77
Calcite	-	-	1.46	1.91	0.01	-	2.39	-
Ankerite	-	-	0.08	-	0.37	-	-	-
Siderite	-	-	0.11	-	0.04	-	-	-
Dolomite	-	-	-	0.29	-	-	-	-
Magnetite /Hematite+Ti	1.43	1.13	1.04	-	1.3	1.35	0.81	0.04
Magnetite/Hematite	0.71	0.18	0.52	0.03	0.42	0.22	0.35	0.65
Ilmenite	0.17	0.08	0.18	0.2	0.1	0.07	0.21	0.23
Sulfide minerals	-	-	0.01	3.36	-	-	-	-
Apatite	0.13	0.13	0.17	0.14	0.18	0.19	0.09	-
Gypsum	0.05	0.07	-	-	-	-	-	0.02
Zircon	-	-	-	-	0.01	0.01	-	0.01
Rhodocrosite	-	-	-	0.03	0.52	-	-	-
Other minerals	1.16	0.4	0.05	0.03	0.03	0.01	0.06	0.56
Non identified	0.01	-	0.44	0.05	0.54	0.18	0.03	-

1062 Table 3: Quantitative evaluation of rock mineral composition from QEMSCAN® analysis.

1063

1064

1065

	H_2O^+ (wt%)	φ_{tw} (%)	φ_{FA} (%)	Permeability k (m²)
PA 1	0.84	7.45	-	$5.8\ 10^{-19}$
PA 2	1.03	4.28	-	$2.77e10^{-19}$
PA 3.1	0.76	3.74	4.31	$1.72\ 10^{-17}$
PA 3.2	1.04	9.46	-	$2.32\ 10^{-19}$
PA 4	1.13	7.33	4.14	$4.5\ 10^{-19}$
PA 5.1	1.18	9.86	-	$3.9e10^{-19}$
PA 7.2	1.91	7.2	4.93	$7.66\ 10^{-20}$
PA 10.1	1.21	13.84	11.21	$2.48\ 10^{-18}$
PA 11	6.23	35.35	20.99	$5.36\ 10^{-17}$
PA 12	2.78	17.05	9.76	$1.61\ 10^{-17}$
PA 13.1	0.65	10.5	6.59	-
PA 13.2	0.93	4.48	4.11	-

1066 Table 4: Crystal lattice water proportions (H_2O^+) from bulk-rock chemical analysis; connected
1067 porosities φ_{tw} and φ_{FA} obtained by triple-weighted method (TW) and from film
1068 autoradiography (FA) respectively and Darcian permeabilities k of samples.

1069

Solution	Sample Number									
	PA.1	PA.2.1.	PA.3.1	PA.3.2	PA .4	PA.5.1	PA.7.2	PA.10.1	PA.11	PA.12
219.40	70.900	87.000	78.700	181.00	81.700	202.90	112.30	486.90	1039.5	1256.3
995.40	87.400	N/A	97.100	246.50	104.80	263.90	147.20	687.00	1772.0	1380.0
1956.7	94.700	116.70	N/A	258.10	109.30	232.80	142.20	614.30	N/A	1428.0
9297.4	133.80	168.40	152.40	369.40	156.60	311.40	185.90	895.30	2283.1	2125.0
17599.0	202.30	263.40	248.00	539.70	237.10	223.00	286.30	1246.9	3236.2	2898.6
31288.0	267.70	366.80	313.50	719.40	326.90	557.40	397.90	1618.1	5434.8	3663.0

1070
1071 Table 5. Conductivities of the solutions saturating the samples and bulk conductivities (expressed in $\mu S.cm^{-1}$).
1072

1073

1074

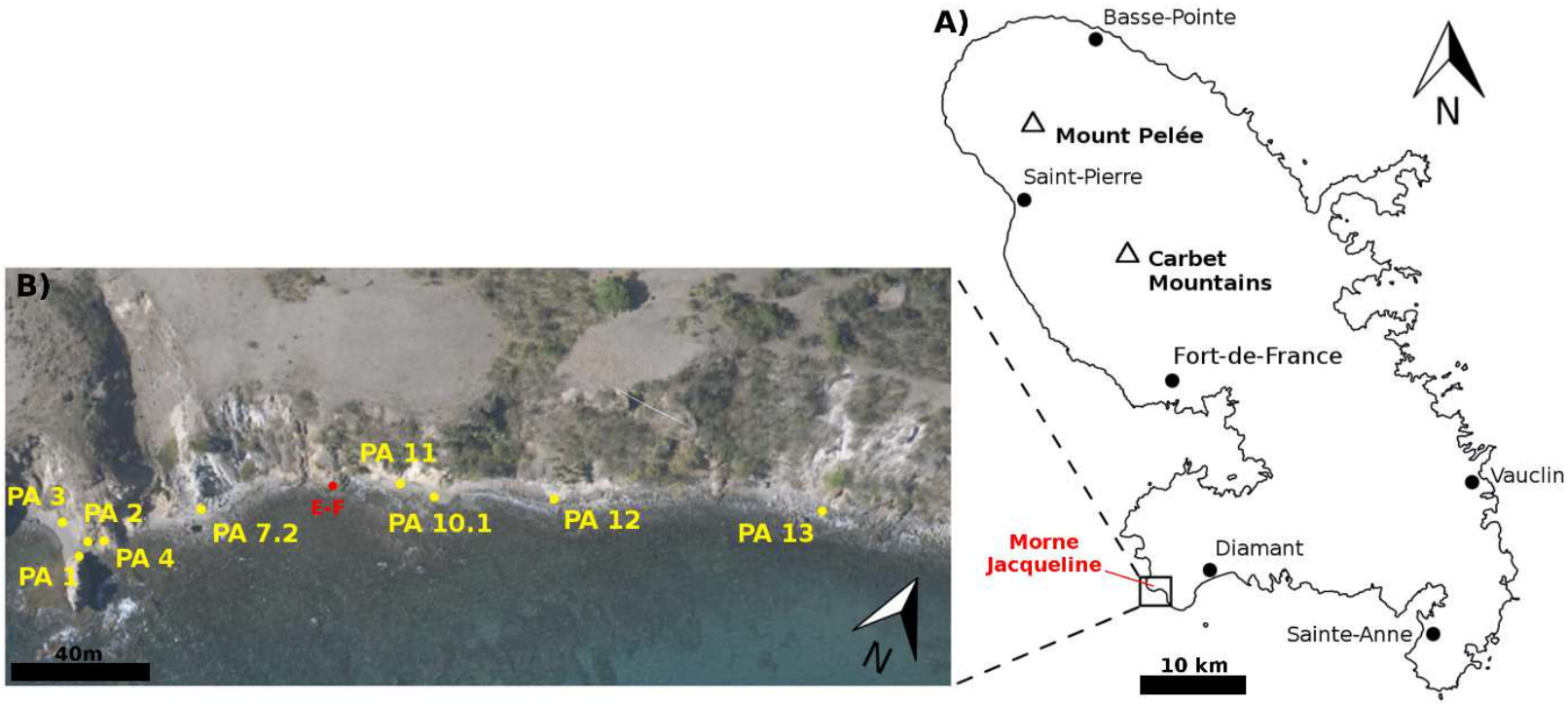

1075

1076 Figure 1: Locations of the Petite Anse-Diamant area on Martinique Island (A) and the samples investigated in this study (B). The red point (E-F)

1077 indicates the location of the Eaux-Ferrées thermal source (source: IGN, French institute of geography).

1078

1079

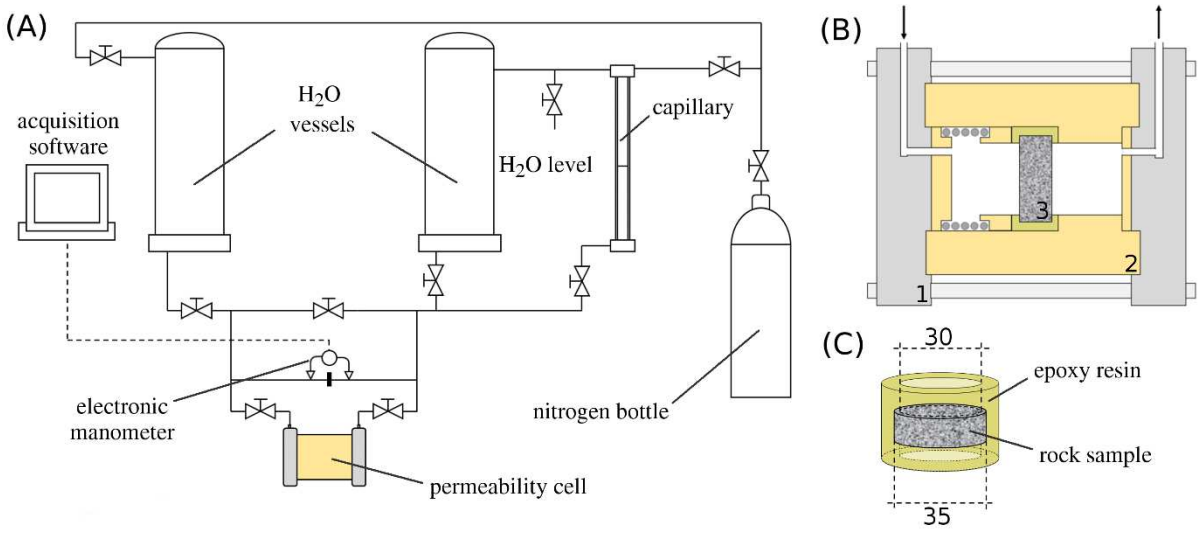

Figure 2: (A) Experimental setup for the permeability measurements (Sammartino et al. 1999). (B) Cross-section of the permeability cell with (1) the pressure vessels of stainless steel, (2) the cell core (in PEEK) and (3) the plug sample. (C) Perspective view of the plug sample with the diameters of the core sample and plug opening (mm).

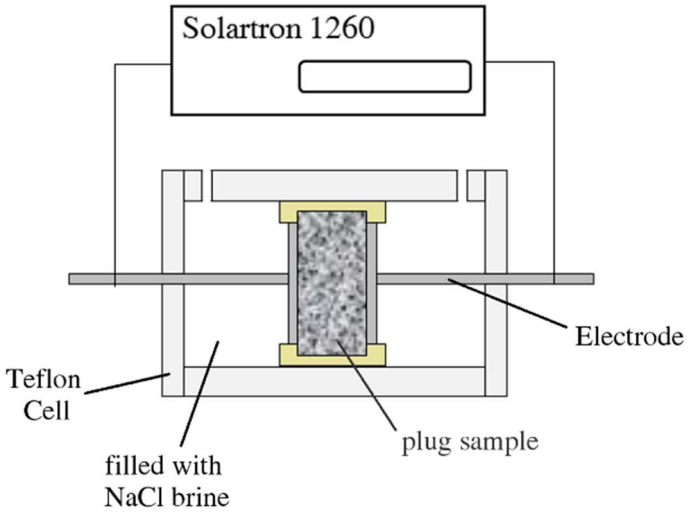

Figure 3: Resistivity cell used for acquisition of the impedance spectra.

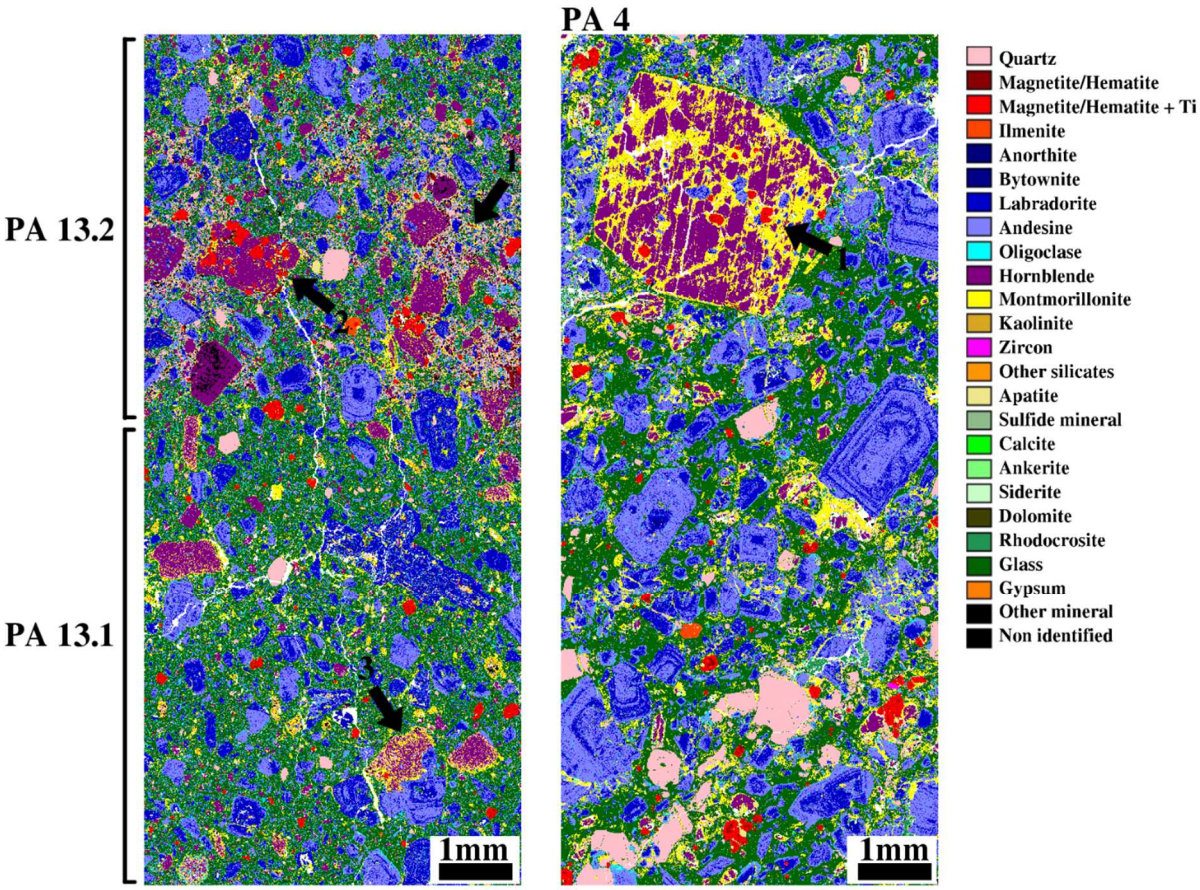
PA 4
PA 13.2
PA 13.1
1
2
3
1mm
1mm
Quartz
Magnetite/Hematite
Magnetite/Hematite + Ti
Ilmenite
Anorthite
Bytownite
Labradorite
Andesine
Oligoclase
Hornblende
Montmorillonite
Kaolinite
Zircon
Other silicates
Apatite
Sulfide mineral
Calcite
Ankerite
Siderite
Dolomite
Rhodocrosite
Glass
Gypsum
Other mineral
Non identified

1096

1097

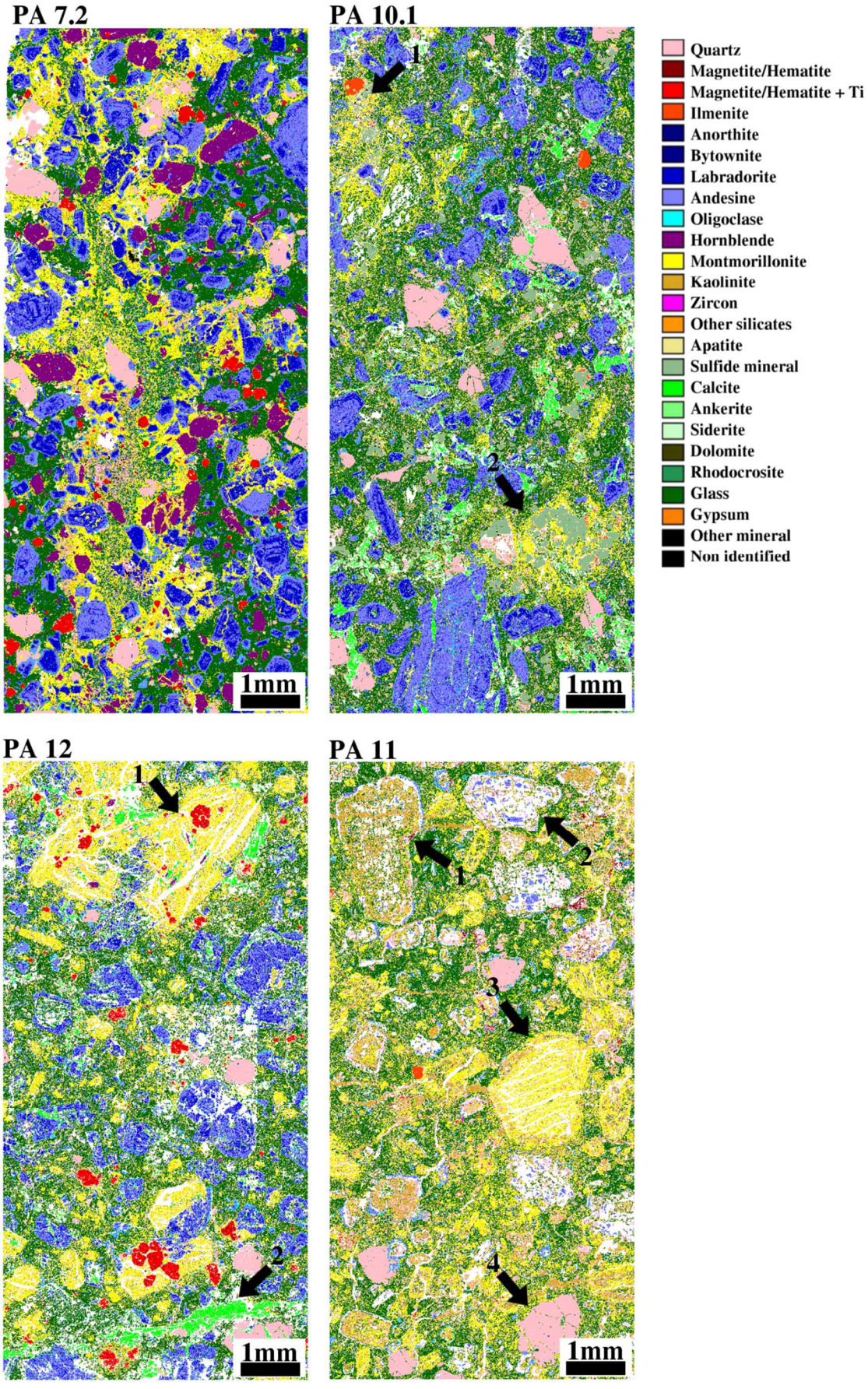
PA 7.2
PA 10.1
PA 12
PA 11
1mm
1mm
1mm
1mm
1
2
1
2
1
2
3
4
Quartz
Magnetite/Hematite
Magnetite/Hematite + Ti
Ilmenite
Anorthite
Bytownite
Labradorite
Andesine
Oligoclase
Hornblende
Montmorillonite
Kaolinite
Zircon
Other silicates
Apatite
Sulfide mineral
Calcite
Ankerite
Siderite
Dolomite
Rhodocrosite
Glass
Gypsum
Other mineral
Non identified

1098

Figure 4: QEMSCAN® mineral maps of samples PA13.2, PA13.1, PA4, PA 7.2, PA10.1, PA12 and PA 11. White areas are pixels detected as porosity. Sample PA13 is the freshest sample of andesite, presenting moderate alteration of hornblende to montmorillonite at the bottom of the section (arrow 3), and silica and oxides abundance in the mesostase (arrows 1 and 2). In sample PA4, intragranular alteration of hornblende crystals is underscored by montmorillonite and oxides in cleavage planes. Sample PA10.1 exhibits pervasive alteration of the mesostase (presence of montmorillonite, silica, and sulphide minerals) (arrows 1,2). In sample PA12, hornblende crystals are totally replaced by montmorillonite and iron oxides (arrow 1); carbonate veins are also detected (arrow 2). Sample PA11 is extremely altered; hornblende is totally replaced by silica and montmorillonite (arrow 3), and feldspars phenocrysts are partially dissolved, containing dissolution voids(arrow 2), which are partially filled with kaolinite and silica (arrow 1). In this sample, quartz grains remains unaltered.

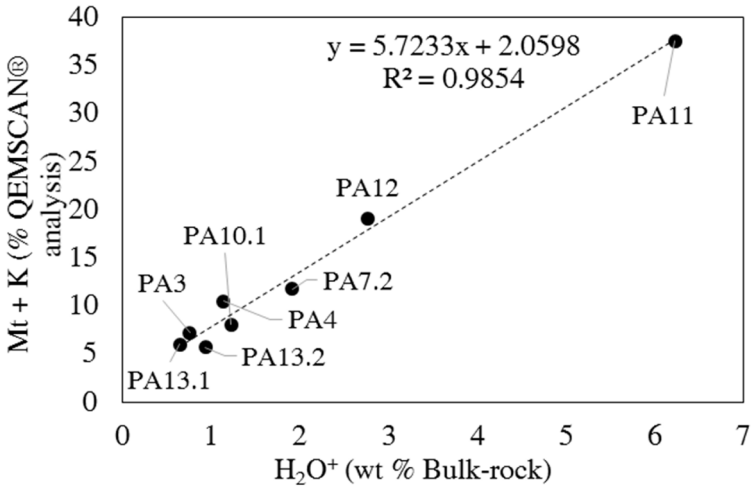

Figure 5: Correlation plot between the abundance of the clay phases identified by the QEMSCAN® system and the crystal lattice water proportions obtained from bulk-rock chemical analysis. Mt = montmorillonite and K = kaolinite.

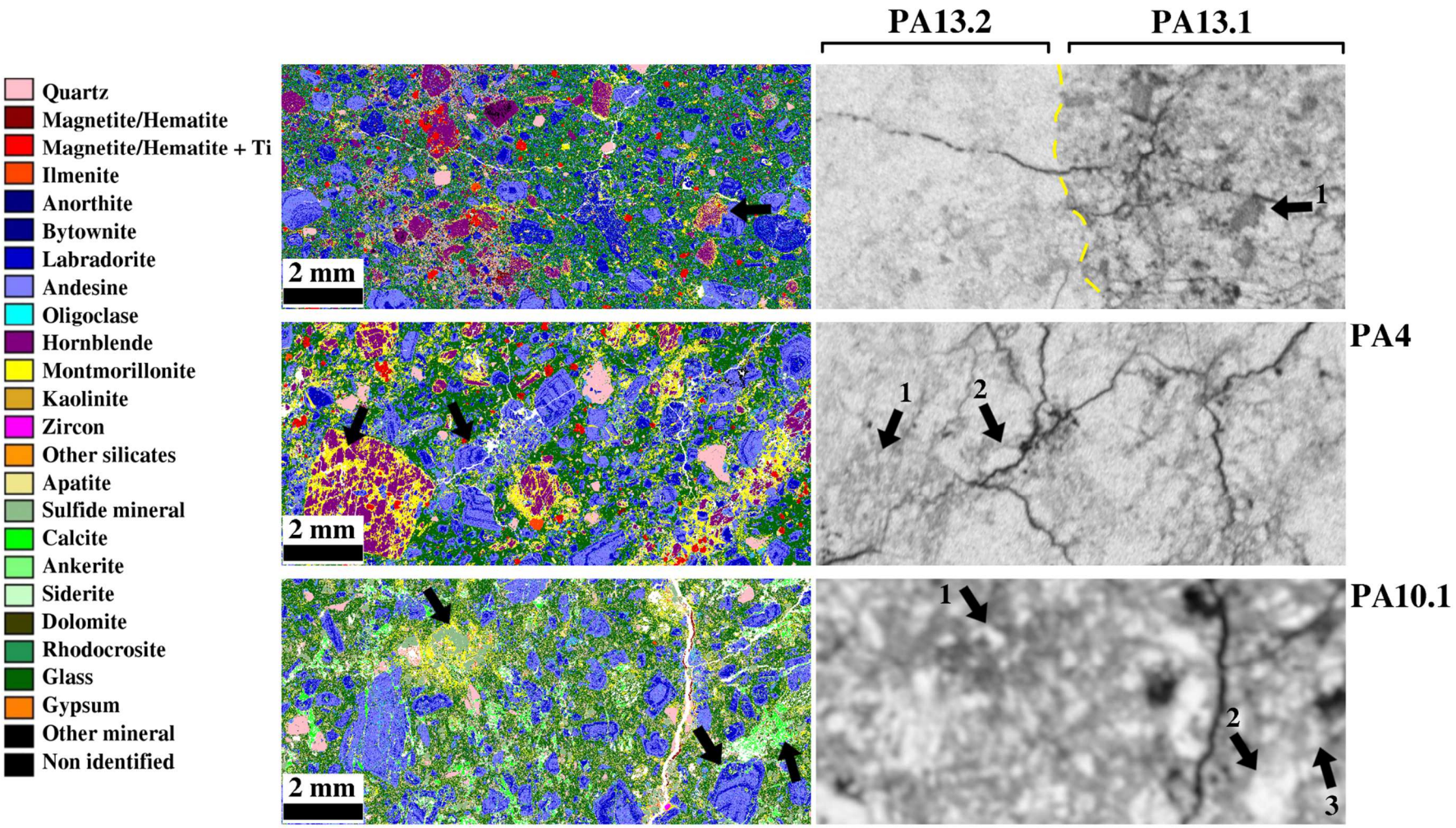
Quartz
Magnetite/Hematite
Magnetite/Hematite + Ti
Ilmenite
Anorthite
Bytownite
Labradorite
Andesine
Oligoclase
Hornblende
Montmorillonite
Kaolinite
Zircon
Other silicates
Apatite
Sulfide mineral
Calcite
Ankerite
Siderite
Dolomite
Rhodocrosite
Glass
Gypsum
Other mineral
Non identified
PA13.2
PA13.1
2 mm
2 mm
2 mm
1
PA4
1
2
PA10.1
1
2
3

1118

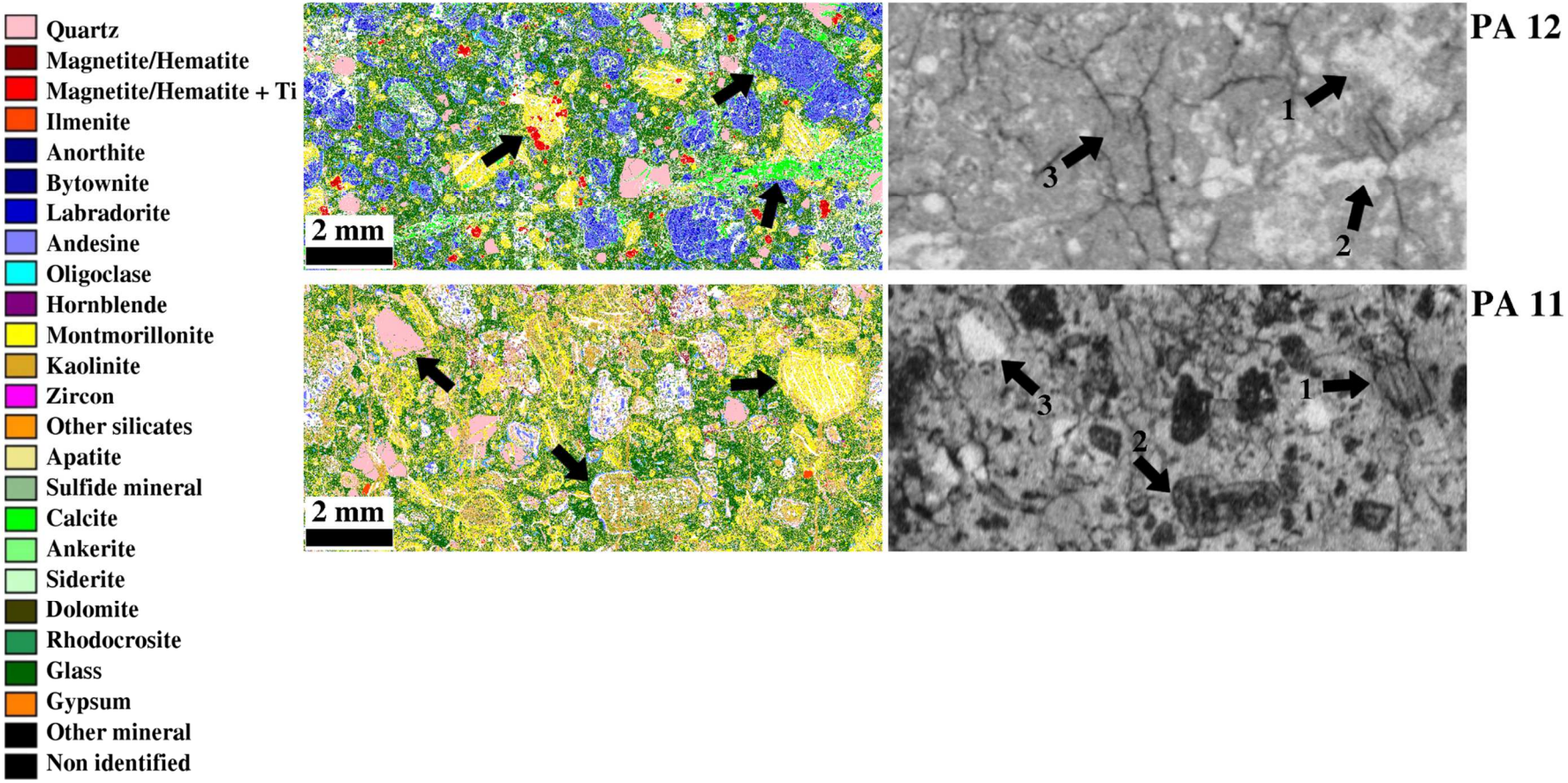

Figure 6: QEMSCAN® Mineral maps (left) and related autoradiographs (right) from the ^{14}C-PMMA method of samples PA 13, PA 4, PA 10.1, PA 12 and PA 11. In autoradiographs, the darker the grey level is, the higher the porosity is. In the freshest sample (PA13) the most porous mineral is hornblende, partially replaced by montmorillonite in PA 13.1 side (arrow 1). In PA4 sample, porosity is well developed in hornblende cleavage planes (arrow 1), and corresponds to montmorillonite; feldspars remains lowly porous (arrow 2). In sample PA 10.1, low porosity area

1124 are initial feldspar phenocrysts (arrow 2), but are also in sulphide of pseudomorphosed hornblende (arrow1) and in carbonate cements.
1125 Montmorillonite-rich areas and in a less extent mesostase present an higher porosity. In PA12, Feldspars remain unaltered and lowly porous
1126 (arrow 1), as well carbonate. High porosity of pseudomorphosed hornblende cannot be differentiate from the porosity of the mesostase (arrow 3).
1127 Sample PA11, which is the most affected by hydrothermal alteration, presents a totally different porosity pattern than sample PA12. In this
1128 sample, quartz grains remains the only lowly porous mineral (arrow 3). The connected mesostase matrix is porous, but pseudomorphosed
1129 hornblende (arrow 1) and altered/dissolved feldspars associated with dissolution voids (arrow 2) are more porous.
1130
1131

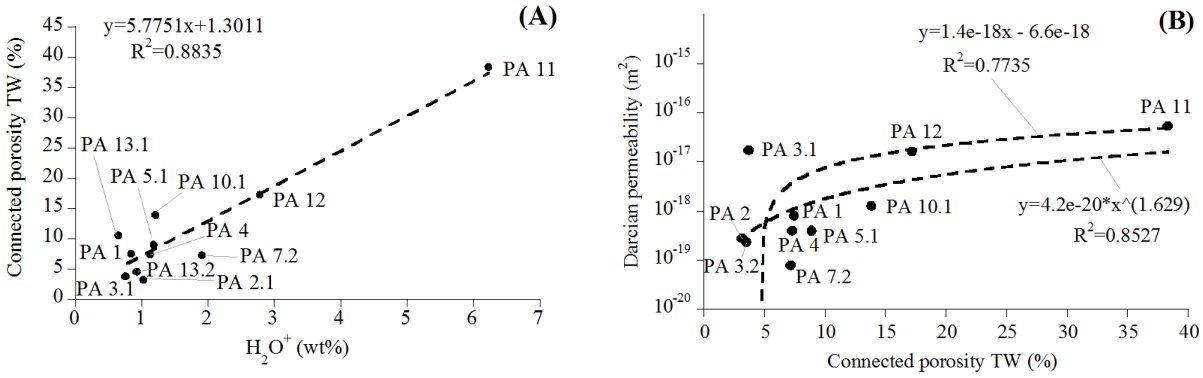

Figure 7: (A) Plot of the connected porosity of the samples against the structural water content (H_2O^+) value obtained with the triple weight (TW) method and from bulk-rock chemical analysis. The H_2O^+ values are used as indicators of the clay mineral abundances (see section 2.2). (B) Intrinsic permeability against the connected porosity.

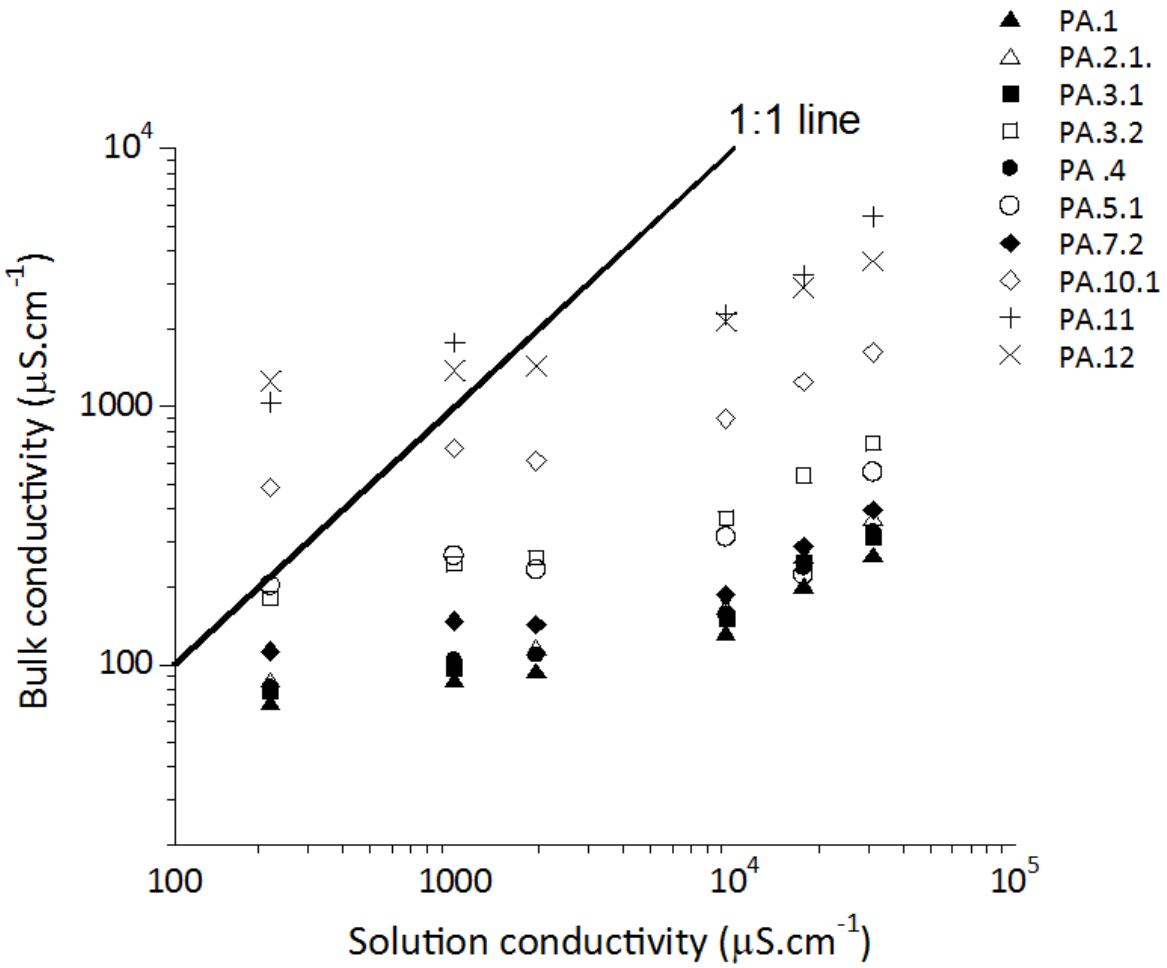

1139

1140 Figure 8: Bulk conductivities versus conductivities of the solutions saturating the samples.

1141 The 1:1 line is used to estimate the isoconductivity point of each sample.

1142

1143

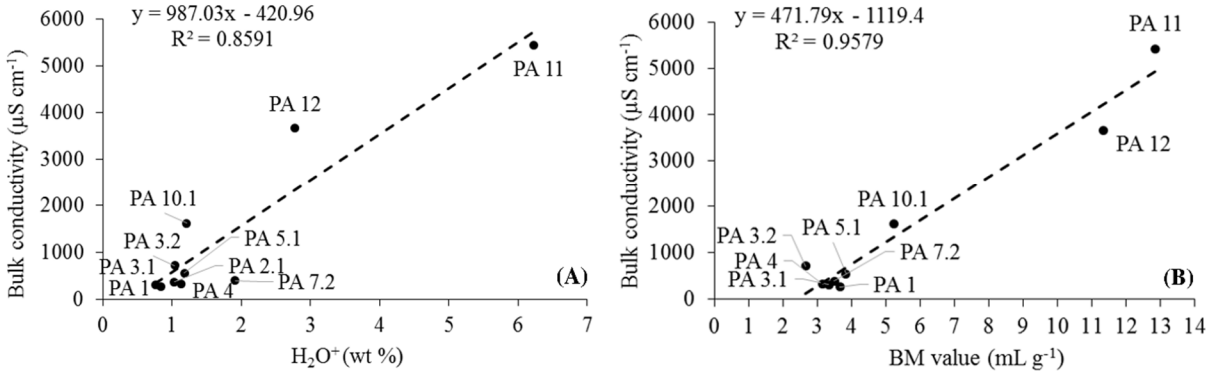

Figure 9: Correlation plots of the bulk conductivity measured for the samples saturated with the 2 wt % NaCl solution depending on the structural water proportion (H_2O^+) (A) and blue methylene (BM) value (B).

1153

1154

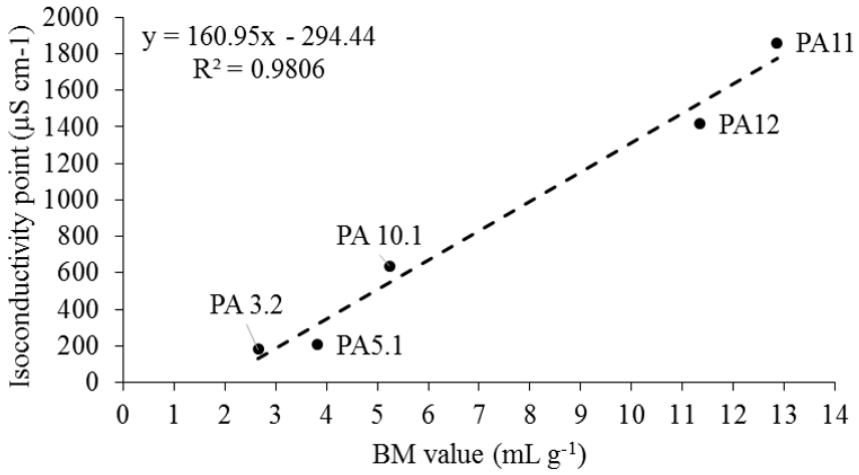

1155

1156 Figure 10: Evolution of isoconductivity point depending on methylene blue value (BM).

1157

1158